ULTRASONIC BACKSCATTER COEFFICIENT QUANTITATIVE ESTIMATES FROM CHINESE HAMSTER OVARY AND BALB/3T3 CELL PELLET BIOPHANTOMS

BY

AIGUO HAN

THESIS

Submitted in partial fulfillment of the requirements
for the degree of Master of Science in Electrical and Computer Engineering
in the Graduate College of the
University of Illinois at Urbana-Champaign, 2011

Urbana, Illinois

Adviser:

Professor William D. O'Brien, Jr.

ABSTRACT

In this study a cell pellet biophantom technique is introduced and applied to the ultrasonic backscatter coefficient (BSC) estimate using Chinese hamster ovary (CHO), and new and old 3T3 cells. Also introduced, for its geometrical similarities to eukaryotic cells, is a concentric sphere scattering model. BSC estimates from cell pellet biophantoms of known number density were performed with 20, 40 and 80 MHz focused transducers (overall bandwidth: 20-100 MHz). These biophantoms were histologically processed and then evaluated for cell viability.

For low cell concentrations, cell pellet BSC estimates were in agreement with the concentric sphere model. Fitting the model to the BSC data yielded quantitative values for the outer sphere and inner sphere. The concentric sphere model thus appears suitable as a tool for providing quantitative information on cell structures and will tend to have a fundamental role in the classification of biological tissues.

For high cell concentrations, the cells are close to each other so that the scattering becomes more complicated. The magnitude and shape of the BSC versus frequency curve, and consequently the parameter estimates from the concentric sphere model, are all affected by the high-concentration effect when the volume density reaches 30%. At low frequencies ($ka<1$), the effect tends to decrease BSC, as is also observed by other researchers. However, what is new in our findings is that the effect could either increase or decrease BSC at frequencies beyond the Rayleigh region. The concentric sphere model least-squares estimates show a decrease in cell radius with number density (15.8, 14.6, 15.1, 13.6, 9.6, 7.1 μm for 1.25, 4.97, 19.7, 72.3, 224, 473 Mcells/mL CHO cell pellets respectively, and 11.4, 9.1 10.7, 8.4 μm for 1.24, 4.84, 17.7,

52.3 Mcell/mL new 3T3 cell pellets, respectively), which indicates that the concentric spheres model starts to break up at large cell concentrations. The critical volume density, starting from when the model becomes inapplicable, is estimated to be between 10% and 30%.

ACKNOWLEDGMENTS

This work would not have been possible without the help and support from many people. First, I would like to thank my adviser, Dr. William D. O'Brien Jr., for giving me the opportunity to start this project, for guiding me throughout the project, for training me to do independent research, for educating me to become a leading expert in the area, and for all his support and encouragement. I must also thank Maxime Teisseire, who originally worked on this project and trained me at the beginning. I would also like to thank the Bioacoustics Research Laboratory, especially Saurabh Kukreti, Michael Kurowski, Matt Lee and Eugene Park for their assistance with data acquisitions and attenuation measurements, Rami Abuhabsah and James P. Blue Jr. for their assistance with cell pellet preparation and Dr. Sandhya Sarwate for her help on histology. Finally, I would like to thank my family for their support. This work was funded by NIH Grant R01CA111289.

TABLE OF CONTENTS

CHAPTER 1

INTRODUCTION

1.1 Quantitative Ultrasound

Ultrasound has been used in diagnostic medical imaging for over 50 years and is still one of the most widely used diagnostic tools. It is a safe, portable, and inexpensive imaging modality, especially when compared with other techniques such as magnetic resonance imaging and computed tomography. The advantages of medical ultrasound motivate the development of new diagnostic techniques using ultrasound. Quantitative ultrasound (QUS), which can display quantitative tissue microstructure information and thus has the potential to become a new technique to classify and diagnose pathologies, has become an active research topic [1].

Conventional ultrasound images are derived from the backscattered radio frequency (RF) echo signals. Typically, the envelope of the echo signals is analyzed and converted to an amplitude-modulated gray-scale B-mode image. Therefore, only the magnitude information of the echo signals is used and the frequency-dependent information is generally not used. However, the frequency content of the echo signals may contain useful information. Properties of the tissue microstructure can potentially be derived from the frequency-dependent information of the echo signals because the echo signals result from scattering by tissue macro- and microstructure with varying acoustic properties (acoustic impedance, etc.). Quantitative ultrasound, in contrast to conventional ultrasound, utilizes the frequency-dependent information to quantify tissue properties such as scatterer size, shape, number density, and acoustic impedance.

In QUS, the backscatter coefficient (BSC) is an important frequency-dependent quantity from which different tissue property parameters can be derived. The BSC and the derived parameters are used to characterize tissues. Therefore, accurate BSC measurement is essential in QUS. BSC describes the effectiveness with which the tissue scatters ultrasound energy, and can be recovered from the frequency-dependent backscattered echo signals [2]. Various techniques have been developed to measure the BSC using single-element transducers [2-9]. These techniques were critical for accurate BSC measurement and made it possible to conduct and compare clinical studies. The BSC technique developed by Chen et al. [2] will be used in this study.

1.2 QUS Models and Biophantoms

There have been successful studies using the frequency-dependent information to characterize tissues. For example, the QUS techniques have been used for differentiating diseased versus healthy tissues, and detecting and classifying cancers. Despite the success achieved in those studies, limitations still exist. It is true that QUS parameters are able to differentiate certain tissues. However, the underlying mechanisms causing the difference in the parameters were not fully understood. Furthermore, the QUS parameters did not successfully match the tissue microstructure. For example, the average acoustic diameter does not match the size of the cell, cell nucleus or any other possible scattering site. These limitations exist because in most tissues the structures responsible for ultrasonic scattering remain unknown and thus models used to extract QUS parameters lack solid foundations. As a model-based imaging approach, QUS requires the identification of scattering sites and appropriate models to accurately describe ultrasonic scattering in tissue.

There have been efforts at understanding the scattering sites and finding the appropriate scattering models. It has been hypothesized that the cell is the dominating scattering site [10]. It was also suggested by researchers that the nucleus could be a significant scattering source [11]. Both hypotheses can be modeled with a fluid-filled sphere model where the cell (or the nucleus) is modeled as a homogeneous fluid sphere embedded in the fluid background having acoustic properties that are different from those of the sphere. In addition to the fluid-filled sphere model, the spherical Gaussian model was also proposed and widely used. The spherical Gaussian model assumes that the scatterer has spatially varying acoustic impedance, the spatial distribution of which follows the Guassian distribution [12]. Additionally, Oelze and O'Brien proposed a more complicated scattering model called the New Cell Model, which assumes spatially uniform acoustic impedance in the nucleus and spatially varying acoustic impedance in the cell cytoskeleton [13].

There have also been efforts at understanding the scattering sites using approaches such as three-dimensional acoustic impedance map (3DZM) [14] and single cell scattering study [15]. The 3DZMs are virtual volumes of acoustic impedance values constructed from histology to present tissue microstructure acoustically. They can be exploited to visualize and identify possible scattering sites [14]. In the single cell scattering study, the scattered signal from the cell was compared to that from a physical sphere of known acoustic properties [15]. Both approaches yielded useful results.

This study will introduce a new technique - the cell pellet biophantom technique, which is used to study the ultrasound scattering from cells and to identify the scattering sites. Live cells of known concentration are placed in a mixture of bovine plasma and thrombin to form a clot, what we call a cell pellet. Three types of cells are studied: the Chinese hamster ovary (CHO, 6.7 μm in cell radius), the new 3T3 (11.3 μm in cell radius), and the old 3T3 (8.4 μm in cell radius) cells. The cell concentration is varied to examine the effect of cell concentration on backscattered signals. Also introduced in this study is the concentric sphere scattering model that is geometrically similar to eukaryotic cells. In this concentric sphere model, the inner sphere models the cell nucleus, whereas the outer sphere models the cytoplasm. BSC estimate from the cell pellet biophantoms is obtained and compared to the concentric sphere model. Fitted model parameters are extracted and compared to the corresponding properties of cells.

CHAPTER 2

ACOUSTIC THEORY

2.1 BSC Theories – Identical Scatterers

Suppose a plane wave of amplitude P_0 is incident on a scattering volume. BSC is defined for large observation distances to the backscattered direction as the power scattered into a unit solid angle divided by the product of the incident intensity and the scattering volume V:

$$\eta(f) = \frac{r^2}{V} \frac{\left\langle \left| p_{scat}(\theta = \pi) \right|^2 \right\rangle}{P_0^2}, \tag{2.1}$$

where r is the distance from the scatterers to the observation point, $\left| p_{scat}(\theta = \pi) \right|$ is the amplitude of the backscattered wave, and $< \ldots >$ denotes ensemble average.

Assuming the coherent field is not taken into account (waves do not interfere), and multiple scattering is ignored, the total intensity is the sum of the individual intensities from a randomly positioned ensemble of n scatterers, which gives:

$$\eta(f) = \frac{n}{V} \frac{r^2 \left| p_{scat}(\theta = \pi) \right|^2}{P_0^2}, \tag{2.2}$$

where the factor $\frac{n}{V}$ can be expressed as $\overline{n}$ corresponding to the number density of the ensemble.

Now consider two types of scatterers (Figure 2.1): a single fluid sphere and two concentric fluid spheres. Suppose a plane wave of amplitude P_0 is incident on a scatterer.

The expression of the scattered acoustic pressure p_{scat} from a single fluid sphere was given by Anderson [16], and that from two concentric fluid spheres was given by McNew et al. [17]. Therefore, the BSC for both scatterer models can be calculated by inserting the appropriate p_{scat} into Equation (2.2).

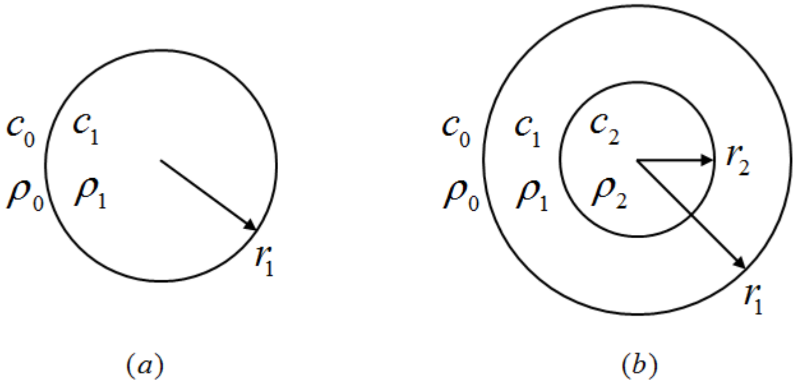

Figure 2.1: Physical properties of single fluid sphere (a), and two concentric spheres (b). For both (a) and (b), the infinite (background) medium has density ρ_o and sound speed c_o. In (a), the sphere has density ρ_1, sound speed c_1 and radius r_1. In (b), the outer sphere has density ρ_1, sound speed c_1 and radius r_1. The inner sphere has density ρ_2, sound speed c_2 and radius r_2. The respective impedances are: $Z_o = \rho_o c_o$, $Z_1 = \rho_1 c_1$ and $Z_2 = \rho_2 c_2$. The three media (inner sphere, outer sphere and background) are each modeled as spatially homogeneous fluids.

The concentric sphere model is applied to the cell pellets. Each cell is modeled as two concentric spheres, the cytoplasm and the nucleus being the outer and inner sphere respectively. Note that the model in Figure 2.1(a) is the aforementioned fluid-fill sphere model, which is shown here to compare with the concentric sphere model.

2.2 BSC Theories – Size Distributions

BSC can be markedly affected by the distribution of scatterer size. Thus it is important to use an accurate size distribution in the model. The Guassian size distribution is used in this study. In fact, direct measurements of the size of the three types of cells (CHO, new and old 3T3) showed that the radii of both the cells and nuclei can be described by Gaussian distributions for each type of cell (Figure 2.2; refer to Section 3.2 for the detailed procedure of cell sizing). Additionally, the cell radius can be assumed to be a linear function of nuclear radius (Figure 2.3) for modeling purposes.

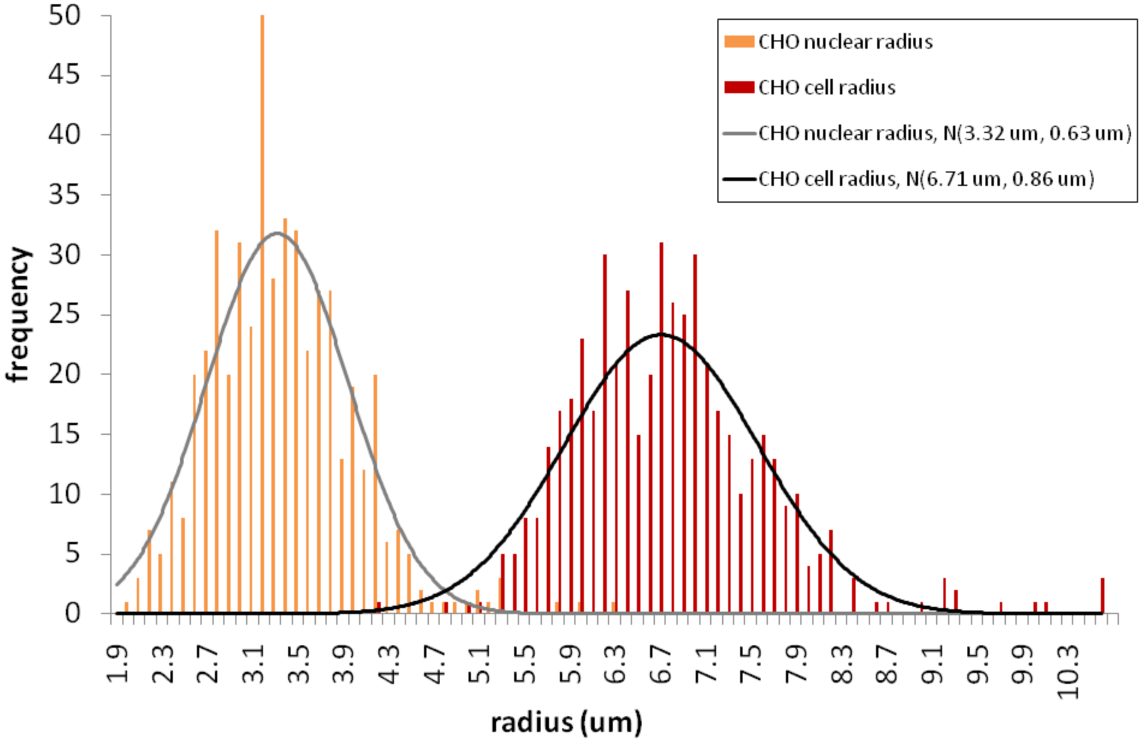

(a)

Figure 2.2: Distributions of CHO (a) and 3T3 (b) cell radius and nuclear radius.

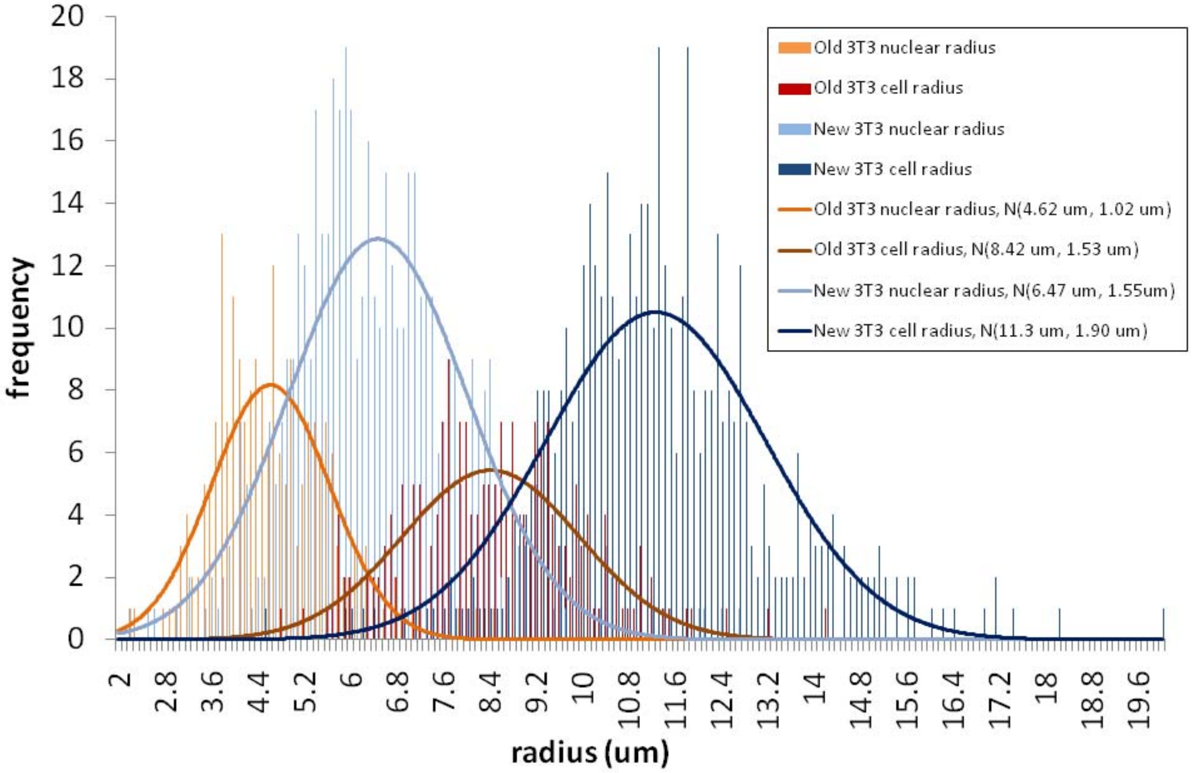

(b)

Figure 2.2 Continued.

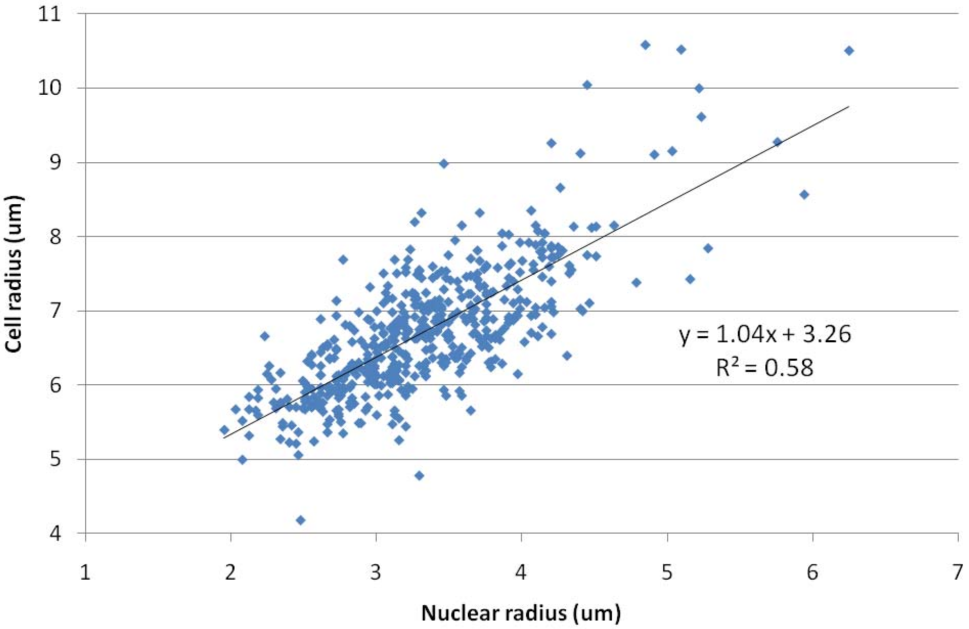

(a)

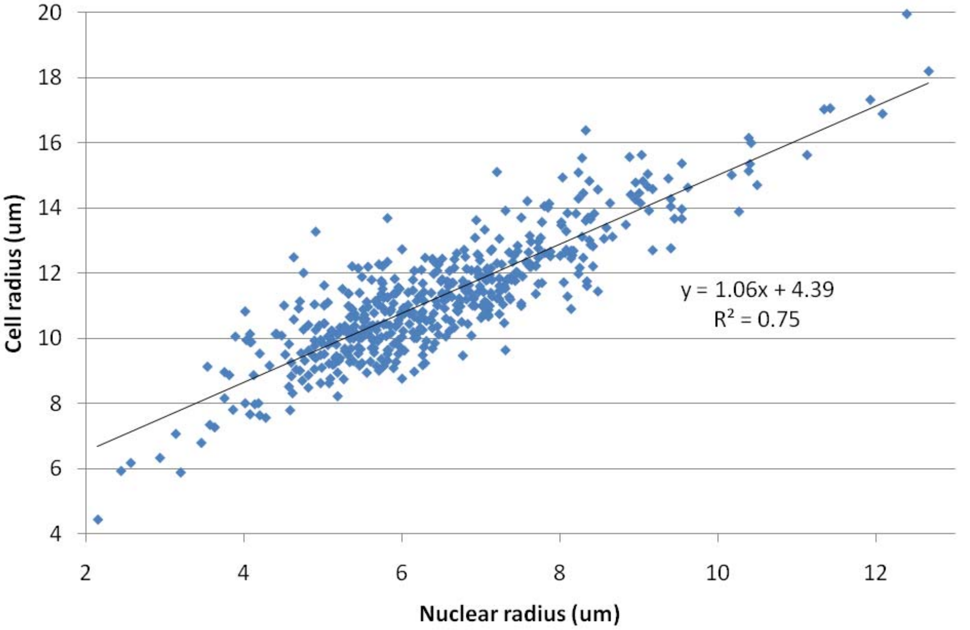

(b)

Figure 2.3: Scatter diagram of (a) CHO, (b) new 3T3, and (c) old 3T3 cell radius and nuclear radius.

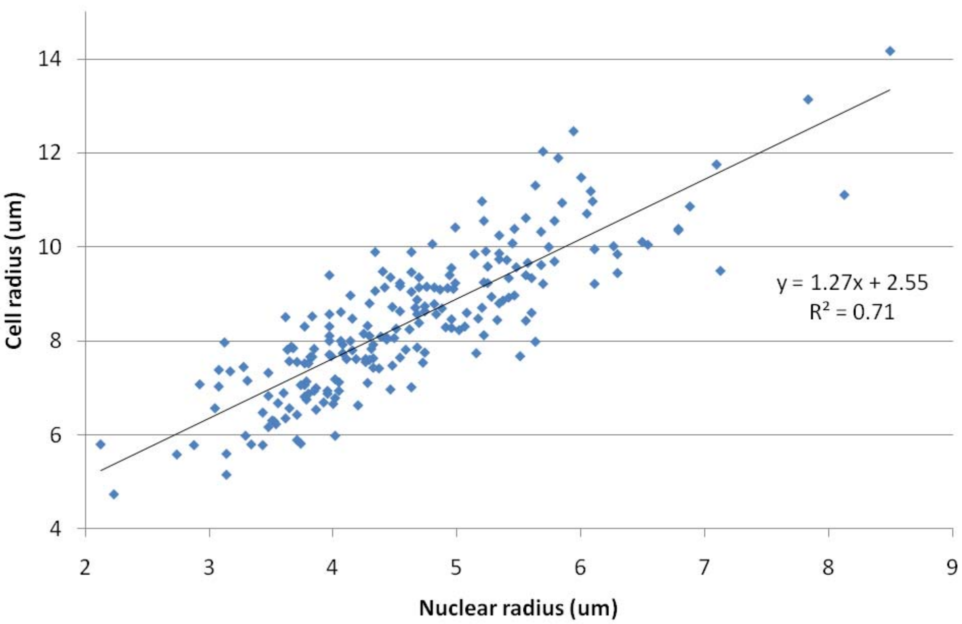

(c)

Figure 2.3 Continued.

For an ensemble of two concentric spheres, if the inner sphere radius has a Gaussian distribution with known mean and standard deviation, and if the outer sphere radius can be expressed as r_1=C_1r_2+C_2 , the theoretical BSC can be computed by

$$\eta_{\mathrm{dist}}(f)=\int_0^\infty g(r_2)\eta(f, C_1r_2+C_2, r_2)dr_2 \ , \tag{2.3}$$

where $g(r_2)$ is the probability density function of the inner sphere radius. For Gaussian size distribution, the effect of size variance on BSC is simulated using Equation (2.3) for the two concentric spheres model and shown in Figure 2.4. The size variance mainly controls the magnitude of the dip at the frequency of around ka = 1 (a is the inner sphere radius). The smallest radii variance yields the largest dip in the high-frequency range, whereas the largest radii variance yields the smallest dip.

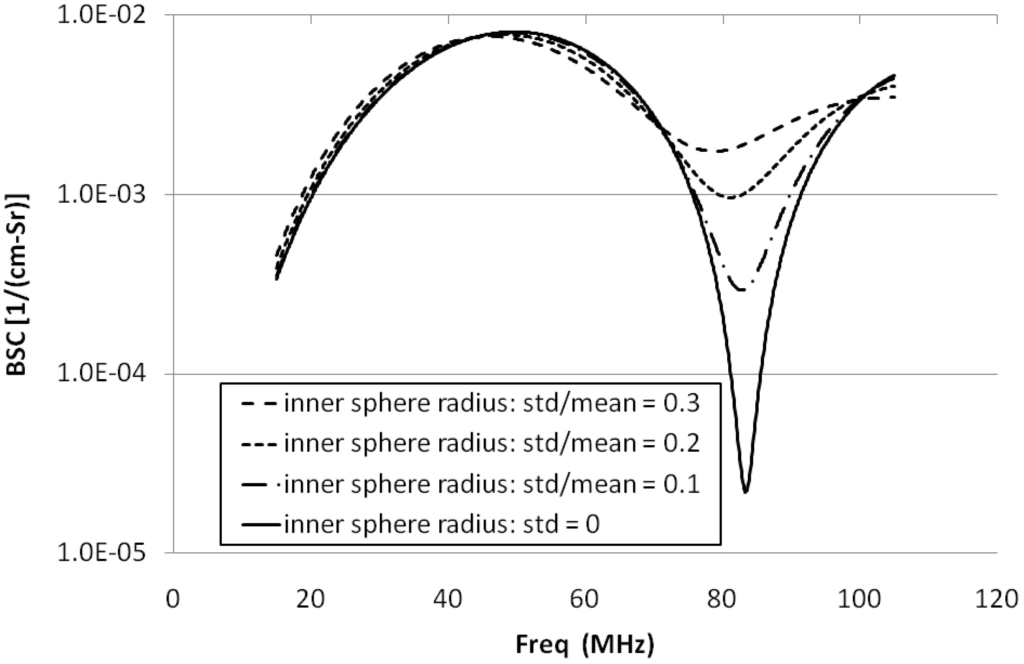

Figure 2.4: Comparison of the theoretical BSC vs. frequency of different size variance for the concentric spheres model. For all the curves, the inner sphere radius r_2 has a Gaussian distribution of mean 3.32 µm. The standard deviation of r_2 is set to be 0, 0.332, 0.664 and 0.996 µm, respectively for each curve, that is, 0, 0.1, 0.2, and 0.3 times the mean. The outer sphere radius r_1 is also assumed to have a Gaussian distribution, and is related to the inner sphere radius by the linear expression $r_1=C_1r_2+C_2$. Thus the mean of the outer sphere radius r_1 is 6.71 µm. As for other parameters, $\overline{n}$=20 million scatterers/mL, Z_1 = 1.58 Mrayl (ρ_1 = 1.03 g/mL, c_1 = 1540 m/s), Z_2 = 1.61 Mrayl (ρ_2 = 1.1 g/mL, c_2 = 1460 m/s) and Z_o = 1.5 Mrayl (ρ_o = 1 g/mL and c_o = 1500 m/s).

CHAPTER 3

METHODS

3.1 Cell Pellet Construction

The cell pellets were constructed by placing live cells (the CHO, the new 3T3 or the old 3T3 cells) in a mixture of bovine plasma and thrombin to form a clot. The clot is called a cell pellet. The detailed procedure of constructing CHO cell pellets was already published [18] and is included here. Chinese hamster ovary (CHO) cells (American Type Culture Collection (ATCC), Manassas, Virginia, USA) were cultured in an F-12K medium (ATCC, Manassas, Virginia, USA) along with 8.98% of fetal bovine serum (Hyclone Laboratories, Logan, Utah, USA) and 1.26% of antibiotic (Hyclone Laboratories, Logan, Utah, USA). A Reichert Bright-Line hemacytometer (Hausser Scientific, Buffalo, New York, USA) was used to count viable cells to yield the number of CHO cells per known volume. Equal volumes of the dye Trypan Blue (HyClone Laboratories, Logan, Utah, USA) and cell suspension (CHO cells in F-12K medium) were gently mixed by pippetting and then added to the counting chambers of the hemacytometer. Trypan Blue was used to differentiate nonviable cells (stained as blue cells) from viable cells (stained as bright cells). At this point, each cell pellet had an average of over 90% live cell viability. A known number of viable cells were placed into a 50 mL centrifuge tube, centrifuged, and the supernatant was removed. 90 μL of bovine plasma (Sigma-Aldrich, St. Louis, Missouri, USA) were added to the cell sediment in the centrifuge tube, which was then vortexed. 60 µL of bovine thrombin (Sigma-Aldrich, St. Louis, Missouri, USA) were added, and the mixture was lightly agitated to coagulate. 0.5 mL of F-12K medium was added to submerse the newly formed pellet. The pellet was transferred to a 1.7 mL microcentrifuge tube that was sealed with Saran Wrap. The F-12K is heated to 37 ˚C prior to its use but other materials are handled at room temperature.

The 3T3 cell pellets were constructed by the following procedure. 3T3 cells (American Type Culture Collection (ATCC), Manassas, Virginia, USA) were cultured in a Dulbecco's Modified Eagle's Medium (DMEM) (ATCC, Manassas, Virginia, USA) along with 8.98% of calf serum (ATCC, Manassas, Virginia, USA) and 1.26% of antibiotic (Hyclone Laboratories, Logan, Utah, USA). A Reichert Bright-Line® hemacytometer (Hausser Scientific, Buffalo, New York, USA) was used to count viable cells to yield the number of 3T3 cells per known volume. Equal volumes of the dye Trypan Blue (HyClone Laboratories, Logan, Utah, USA) and cell suspension (3T3 cells in DMEM medium) were gently mixed by pippetting and then added to the counting chambers of the hemacytometer. Trypan Blue was used to differentiate nonviable cells (stained as blue cells) from viable cells (stained as bright cells). At this point, each cell pellet had an average of over 95% live cell viability. A known number of viable cells were placed into a 50 mL centrifuge tube, centrifuged, and the supernatant was removed. 90 µL of bovine plasma (Sigma-Aldrich, St. Louis, Missouri, USA) were added to the cell sediment in the centrifuge tube, which was then vortexed. 60 µL of bovine thrombin (Sigma-Aldrich, St. Louis, Missouri, USA) were added, and the mixture was lightly agitated to coagulate. 0.5 mL of DMEM medium was added to submerse the newly formed pellet. The pellet was transferred to a 1.7 mL microcentrifuge tube that was sealed with Saran Wrap. The DMEM is heated to 37 ˚C prior to its use but other materials are handled at room temperature.

3.2 Cell Sizing

The following procedure was used to determine the size of the CHO cells [18]. The cells were washed with Dulbecco's Phosphate Buffered Saline (Sigma-Aldrich, St. Louis, Missouri, USA) and covered with 0.25% Trypsin-EDTA solution (Sigma-Aldrich, St. Louis, Missouri, USA). The cell culture flask was immediately placed onto an inverted microscope (Olympus CKX41, Optical Analysis Corporation, Nashua, NH, USA) with a microscope digital camera (Olympus DP20, Optical Analysis Corporation, Nashua, NH, USA). The cells were exposed to Trypsin-EDTA for 10 minutes at room temperature. At this point in time, the cells appeared round and very loosely attached to the flask. Using the camera that is in sync with the microscope, multiple 20X TIF format pictures were taken at varying locations within the flask. Each image contained a 20 μm measure bar. Pictures were no longer taken once the flask had been exposed to Trypsin-EDTA for 18 minutes. The TIF images were opened using Adobe Photoshop CS3. Approximately 25-30 cells were numbered per image using the count tool. These cells were randomly picked based on the criteria that they have a visibly defined cell outer boarder as well as a visibly defined nucleus. These cells were measured (in pixels) along the x and y axis of both the cell and the cell nucleus. The measurement of each parameter was obtained by using the ruler tool and recorded for analysis. The length of the 20 μm measure bar was also measured in pixels as a control. These measurements were taken for 500 samples of the CHO cells, averaged, and converted from pixels to microns.

A similar procedure was used to measure the sizes of the new and old 3T3 cells. A total of 500 new 3T3 cells and 209 old 3T3 cells were measured.

3.3 Data Acquisition

The CHO cell pellet biophantoms were ultrasonically scanned using two single-element transducers (40 and 80 MHz) (NIH High-frequency Transducer Resource Center, University of Southern California, Los Angeles, California USA; see Table 3.1). The 3T3 cell pellet biophantoms were scanned using the three transducers listed in Table 3.1.

Table 3.1: Transducer information and characteristics

Center frequency (MHz)	-10 dB bandwidth (MHz)	Wavelength at center frequency (μm)	f-number	Depth of field (mm)	Beam width (μm)	Acquisition step size (μm)
20	9–33	75.0	3.0	4.0	230	110
40	26–65	37.5	3.0	2.4	113	60
80	49–105	18.8	3.0	1.2	56.4	30

The transducers were driven using a UTEX UT340 pulser/receiver (UTEX Scientific Instruments Inc., Mississauga, Ontario, Canada) which operated in the pitch-catch mode (Figure 3.1). A 50DR-001 BNC attenuator (JFW Industries Inc., Indianapolis, IN, USA) was connected to the pulser to attenuate the driving pulse in order to avoid transducer saturation. An RDX-6 diplexer (Ritec Inc., Warwick, RI, USA) was used to separate the transmitted and received signals because only the transmitted signal needs to be attenuated. The transducers were moved using a motion control system (Daedal Parker Hannifin Corporation, Irwin, Pennsylvania, USA) that has a linear spatial accuracy of 1 μm. The analog echo signal was processed using a 10-bit Agilent U1065A-002 A/D card (Agilent Technologies, Santa Clara, California, USA) set to sample at 1 GHz.

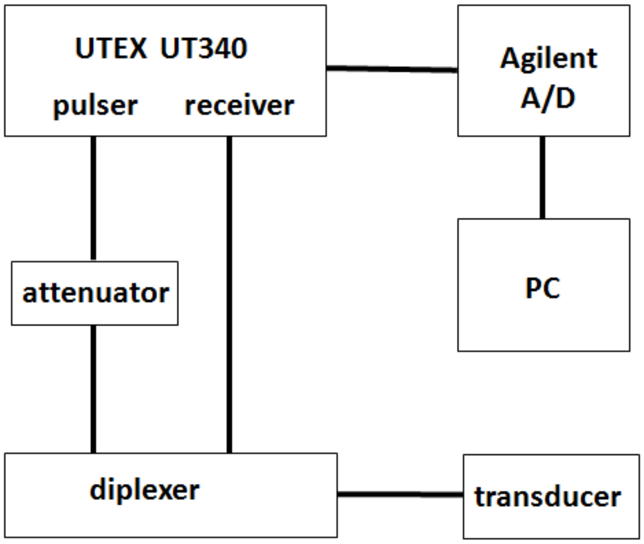

Figure 3.1: Block diagram of the electronic components of the system.

Scans were performed in a tank filled with degassed water having a temperature between 21.5 and 22.5 ˚C. The transducer focus was positioned in the cell pellet. The focal volume was of sufficient length that several regions of interest (ROIs) could be acquired and processed from each scan. Each cell pellet yielded 11 independent scans. Each independent scan could yield a B-mode image if the envelop was detected. More RF signals were obtained at the higher center frequency because higher frequencies yield a weaker signal and consequently the BSC estimates at higher frequencies were somewhat noisier.

3.4 Data Processing

The BSCs were computed from the RF echo data using the planar reflection technique developed by Chen et al. [2]. This method was designed to remove equipment-dependent effects by dividing the power spectrum of the measured data by a reference spectrum. Reference signals were obtained using the specular reflection from Plexiglas placed at the transducer focus in degassed water. Plexiglas has a frequency-independent pressure reflection coefficient of 37% relative to 22 ˚C water. Cell pellet attenuation compensation and Saran transmission compensation were also performed when estimating the backscattered power spectra.

To generate the BSC versus frequency cell pellet estimate from a single transducer, (1) a BSC estimate was made for each ROI using an ensemble average of RF echo signals from that ROI, (2) these ROI BSCs from one of the 11 independent scans were averaged and then (3) the 11 BSCs were averaged.

The best fit to the concentric sphere model was performed by minimizing the sum of the squares of the difference between theoretical and experimental BSCs. A least-squares analysis was used to determine the parameters that best agreed with the experimental response in the spectral domain. Gaussian distributions were applied to both the cell and nuclear radii. The mean and standard deviation of the nuclear radius were assumed to be linked by std/mean equaling 0.19, 0.24 and 0.22 for CHO, new 3T3 and old 3T3, respectively, as suggested by the real measurements of the CHO and 3T3 nuclear sizes (Figure 2.3). The cell radius is linked to the nuclear radius by $r_1 = C_1 r_2 + C_2$, where C_1 and C_2 are parameters to be fitted. Therefore, the parameters are μ_2 (the mean of nuclear radius), C_1 , C_2 , ρ_1, ρ_2, c_1, c_2, and $\bar{n}$. The background medium was assumed to have an impedance Z_0 = 1.5 Mrayl (ρ_0 = 1 g/mL and c_0 = 1500 m/s). Even though the number density $\bar{n}$ is a quantified parameter, it is still treated as an unknown parameter in the minimization procedure, functioning as a gain factor accounting for possible BSC magnitude uncertainties introduced by the measurement method and the attenuation compensation bias.

The problem of fitting multiple parameters was solved by the MATLAB (The Mathworks Inc., Natick, Massachusetts, USA) nonlinear curve-fitting function "lsqcurvefit", wherein the trust-region-reflective algorithm was used as the nonlinear data-fitting approach.

3.5 Biophantom Evaluation

The scans were completed within two hours after clot formation. Immediately after scanning, the cell pellet was removed from the microcentrifuge tube, placed into a histology processing cassette and fixed by immersion in 10% neutral-buffered formalin (pH 7.2) for a minimum of 12 hours for histopathologic processing. The pellet was then embedded in paraffin, mounted on glass slides and stained with hematoxylin and eosin (H&E) for routine microscopic (Olympus BX−51, Optical Analysis Corporation, Nashua, NH, USA) evaluation by a pathologist. Figure 3.2(a) shows a series of isolated cells. Concentric sphere geometry structure as well as cell and nuclear sizes are visible.

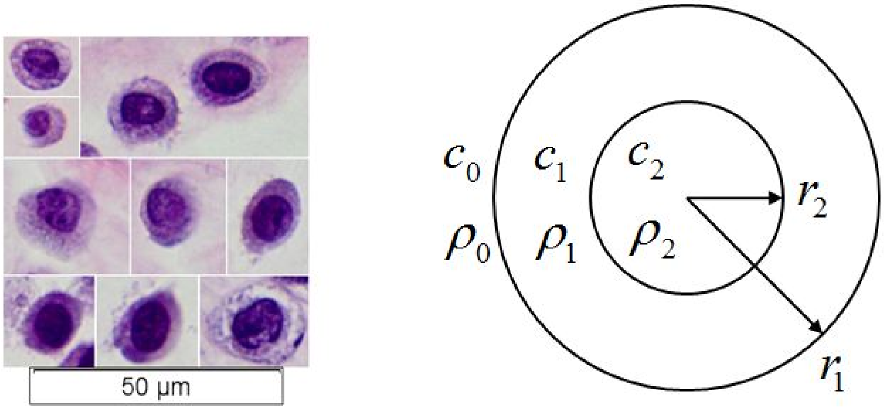

(a) (b)

Figure 3.2: Comparison between (a) optical microscope images (40x) of H&E stained CHO cells and (b) the concentric sphere model. Figures are adapted from [18].

3.6 Cell Pellet Attenuation Measurements

Attenuation compensation is essential for this study because the attenuation is large at high frequencies and the fitted model parameters can be very sensitive to the magnitude and shape of the BSC versus frequency curves. The attenuation of the cell pellets is measured using the insertion loss method and broadband technique with two transducers (the 40 and 80 MHz transducer in Table 3.1). At the 20 – 100 MHz frequency range, the effect of water attenuation is not negligible in the measurement. Therefore, the following equation is used to calculate cell pellet attenuation:

$$\alpha(f) = \alpha_w(f) + \frac{20}{2d_z}\log_{10}\left(\frac{S_r(f)}{S_p(f)}\right), \tag{3.1}$$

where $\alpha(f)$ is the frequency-dependent attenuation (dB/cm) of the cell pellet, and $\alpha_w(f)$ is the attenuation of the F-12K medium, taken to be similar to water [19]:

$$\alpha_w(f) = 8.6826\times10^{-5}(55.9 - 2.37T + 0.0477T^2 - 0.000348T^3)\ \mathrm{dB/cm/MHz^2}\cdot f^2\,, \quad (3.2)$$

where T is the temperature (ºC), d_z is the thickness of the cell pellet, and f is the frequency (MHz). $S_r(f)$ is the amplitude spectrum of the reference signal, the signal reflected back from a flat metal surface without the presence of the cell pellet. $S_p(f)$ is the amplitude spectrum of the reflected signal from the metal surface when the cell pellet is placed between the transducer and the metal surface.

3.7 Transmission Compensation

A 10-µm-thick plastic film (Saran Wrap; Reynolds, Richmond, VA, USA) was used to wrap the cell pellet. The ultrasonic transmission properties of the Saran layer were measured and employed in the transmission compensation of BSC calculation. The transmission coefficient versus frequency curve (Figure 3.3) of the three-layer media (water-Saran-water) was measured using the broadband technique from 1 to 100 MHz. First, a reference signal was obtained using the specular reflection from Plexiglas placed at the transducer focus in degassed water. Then, a layer of Saran was inserted to the ultrasonic pathway and was held such that the Saran was parallel to the Plexiglas surface. The distance between the Saran and Plexiglas surface was 1.6 mm so that the diffraction caused by the insertion of Saran was negligible. The following equation is used to calculate transmission coefficient through water-Saran-water interface (round-trip, the pulse transmitted through the Saran layer twice in this experimental setup):

$$T(f) = \frac{S_S(f)}{S_r(f)}, \tag{3.3}$$

where $T(f)$ is the frequency-dependent transmission coefficient, $S_r(f)$ is the amplitude spectrum of the reference signal, and $S_S(f)$ is the amplitude spectrum of the reflected signal from the Plexiglas when the Saran is placed above the Plexiglas. The measured curve is not a cosinusoid-like curve as predicted by the three-layer transmission theory. This might be due to the nonlinearity of the materials and system, the shear wave generated in the Saran, as well as other possible reasons. The measured curve was directly used for transmission compensation, without being fitted to any theoretical model.

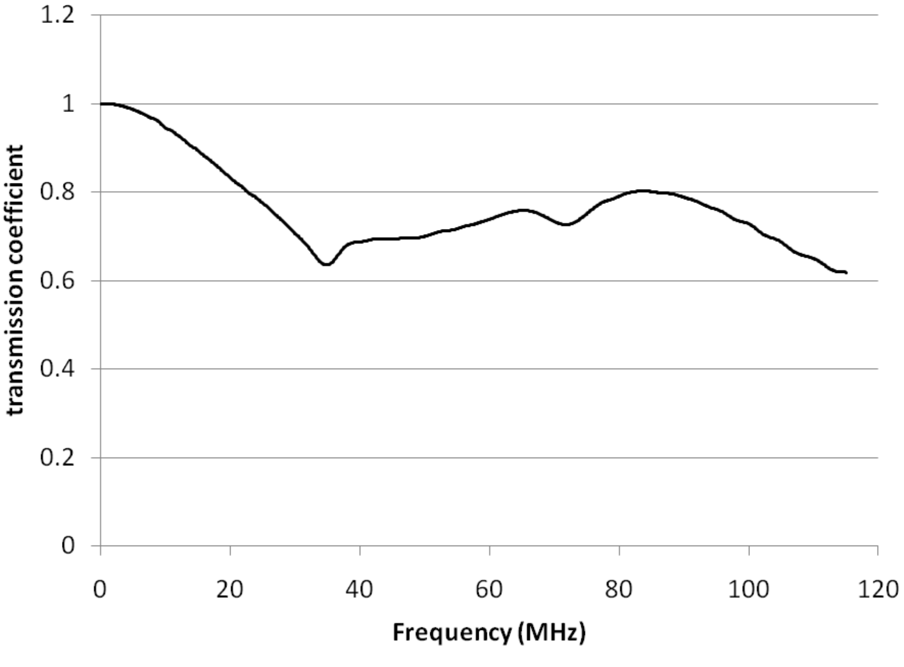

Figure 3.3: Round-trip water-Saran-water transmission coefficient vs. frequency. Individual curves from transducers of different center frequencies have been combined.

CHAPTER 4

RESULTS – CHO CELL PELLETS

4.1 Cell Concentration

Eighteen CHO cell pellets of six different cell concentrations were evaluated (three cell pellets per concentration). The cell concentration is represented by number density and volume density (Table 4.1).

Table 4.1: Summary of cell concentrations of the CHO cell pellets

	Number density (Mcell/mL)	Volume density (mL/mL)
Concentration 1	1.25	0.0017
Concentration 2	4.97	0.0066
Concentration 3	19.5	0.026
Concentration 4	72.3	0.096
Concentration 5	224	0.30
Concentration 6	473	0.63

The number density is defined as the number of cells per unit volume of total mixed materials, i.e.

$$\bar{n} = \frac{N}{V_{cells} + V_{plasma} + V_{thrombin}}, \tag{4.1}$$

where N is the total number of cells, V_{plasma} and $V_{thrombin}$ are the volumes of plasma and of thrombin, respectively, and V_{cells} is the estimated volume of total cells. The volume of one cell is calculated using a sphere radius of 6.71 µm (Figure 2.2).

The volume density (or volume fraction) is defined as the ratio of cell volume to pellet volume, where the volume of cells and the volume of the cell pellet are determined using the method described for the number density. Volume density reveals straightforwardly how close the number density is to the limit. Note that the higher concentrations are close to the upper limit of unity.

The cell concentration is also presented by the histology photos in Figure 4.1. The figure shows that 1.25 and 4.97 Mcell/mL are indeed low cell concentrations, whereas the concentration of 473 Mcell/mL cell pellet is indeed close to the limiting case.

4.2 Cell Pellet Attenuation

The cell pellet attenuation versus frequency curves of the high concentration CHO cell pellets at various cell concentrations are shown in Figure 4.2. For the three lower concentrations (1.25, 4.97, 19.5 Mcell/mL), the attenuation is close to that of the 0 Mcell/mL case. Therefore, the attenuation value of the 0 Mcell/mL case is used for the three lower concentration cases for simplicity.

The following equation is fitted to the cell pellet attenuation versus frequency curves:

$$\alpha(f) = \beta f^{n}, \tag{4.2}$$

where $\alpha(f)$ is in dB/cm, and f is in MHz. The fitted parameters β and n for various concentrations are listed in Table 4.2.

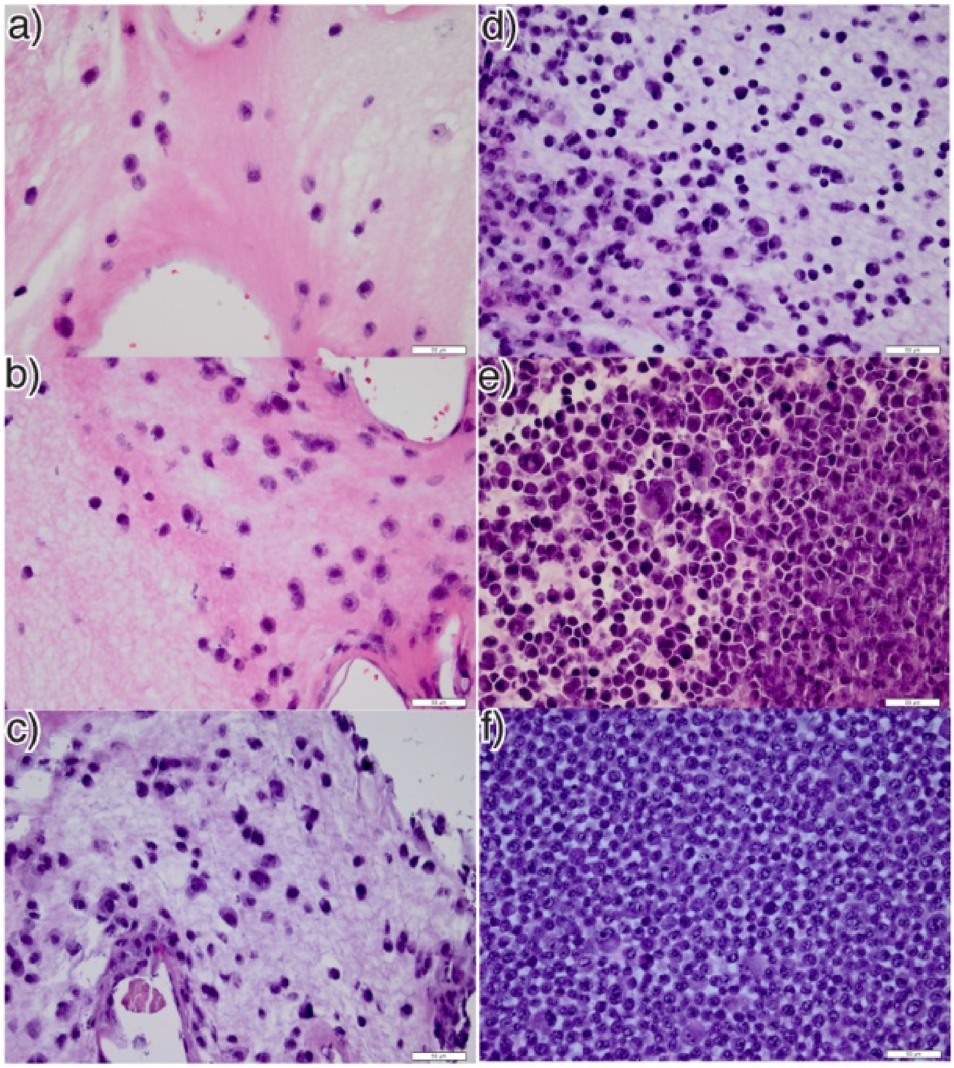

Figure 4.1: Optical microscope images (40X) of H&E stained CHO cells from: CHO cell pellets of number density 1.25, 4.97, 19.5, 72.3, 224, 473 Mcell/mL respectively (a-f). Scale bars represent 50 µm.

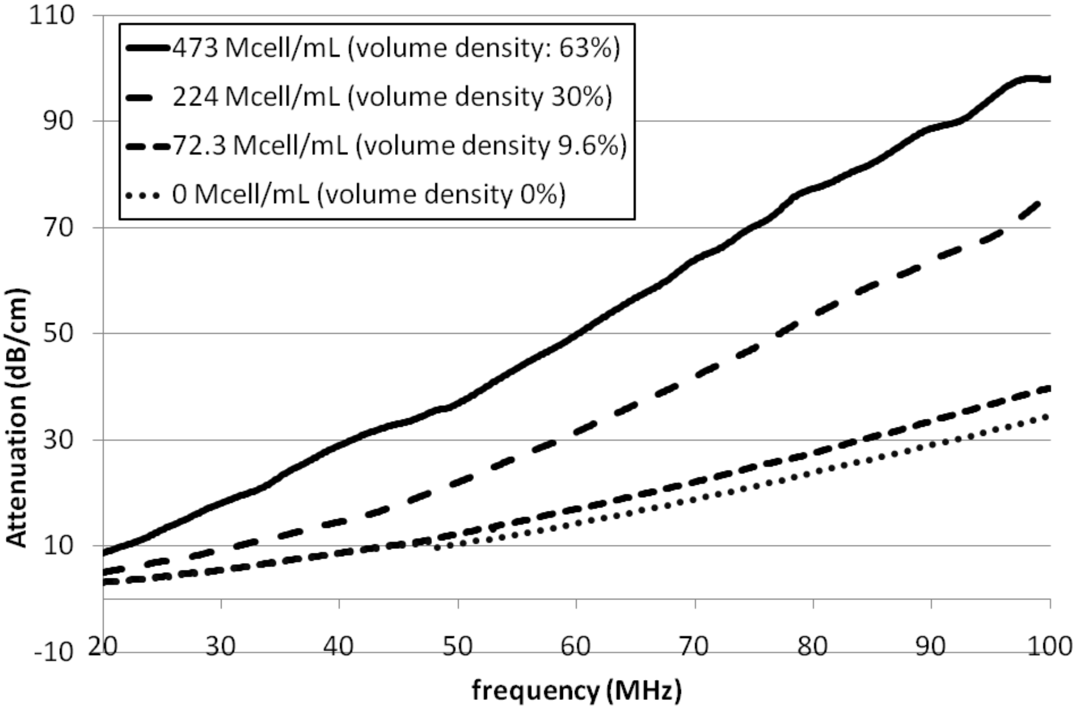

Figure 4.2: CHO cell pellet attenuation vs. frequency.

Table 4.2: Summary of the CHO cell pellets attenuation coefficient for various cell concentrations

Number density (Mcell/mL)	β	n
0	0.021	1.6
72.3	0.019	1.7
224	0.025	1.7
473	0.15	1.4

4.3 BSC versus Frequency

BSC estimates of all the CHO cell pellets are shown in Figure 4.3. The BSC versus frequency curves for different concentrations share a similar pattern in the sense that a consistent peak (crest) at about 55 MHz in the BSC magnitude is followed by a consistent peak (trough) at around 90 MHz. In spite of that, the BSC changes with number density: the BSC magnitude increases with number density, the range of BSC increases with number density, and the positions of the peak and dip vary slightly with number density. Number density affects both the magnitude and the shape of BSC.

4.4 Least-Squares Parameter Estimates

The best fit theoretical BSCs of all samples are calculated using the least-squares technique. Figure 4.4 gives the reader a sense of how the fitted curves are compared to the measured data.

The estimated parameters of the concentric sphere model are summarized in Figure 4.5. The mean values are averages of the three cell pellets for each cell concentration. The standard deviations are also calculated based on the three samples per concentration.

The estimated values of cell radius and nuclear radius are comparable to the directly measured values. The estimated cell radii agree well with the direct measurement for low-concentration conditions (1.25, 4.97, 19.5, 72.3 Mcell/mL), showing that the combination of concentric spheres model and least-squares method makes it possible to predict cell radius using the BSC information. For higher concentration cell pellets

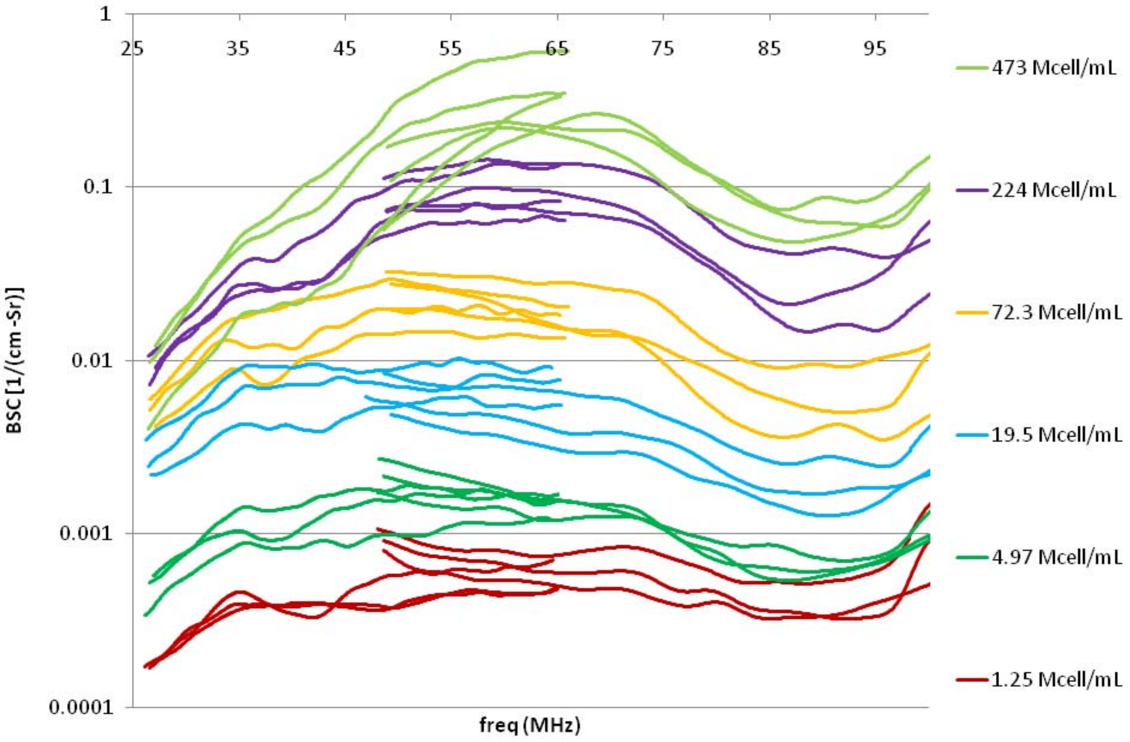

Figure 4.3: Estimated BSC vs. frequency for all CHO cell pellets. Estimated BSC of each cell pellet sample is based on data acquired from two transducers: 40 MHz and 80 MHz. The legends represent number density. There are three cell pellets per number density.

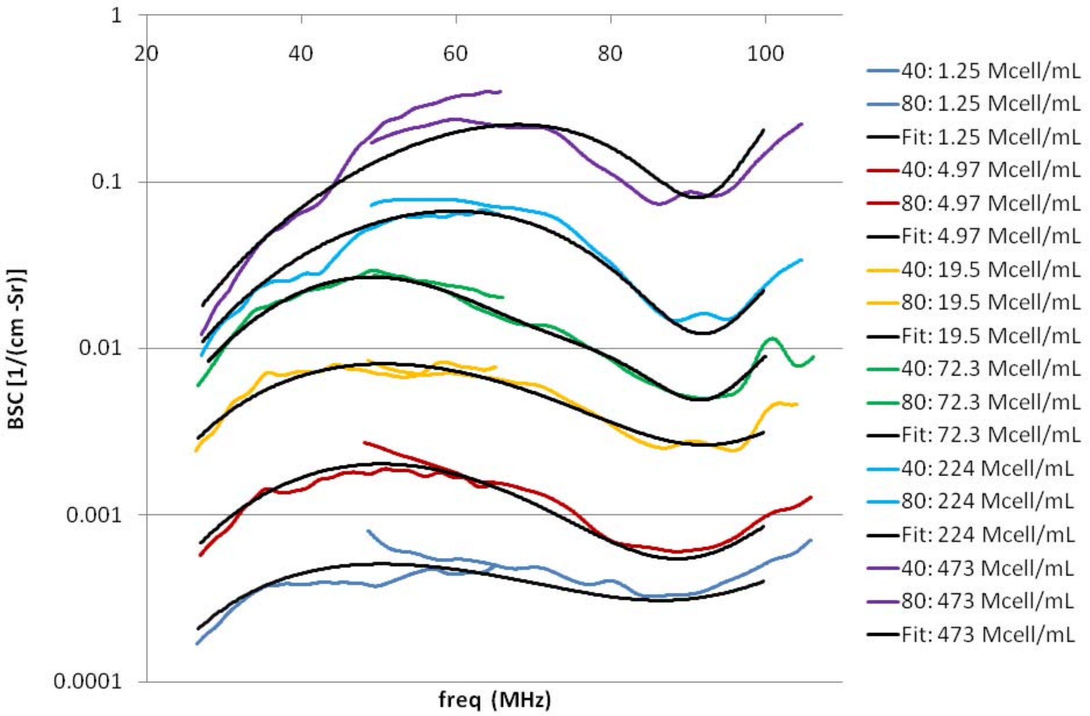

Figure 4.4: Fitted BSC of CHO cell pellets compared with measured data. The black lines represent the fitted BSC relative to the concentric sphere model. Only one representative cell pellet sample per number density is shown for figure simplicity.

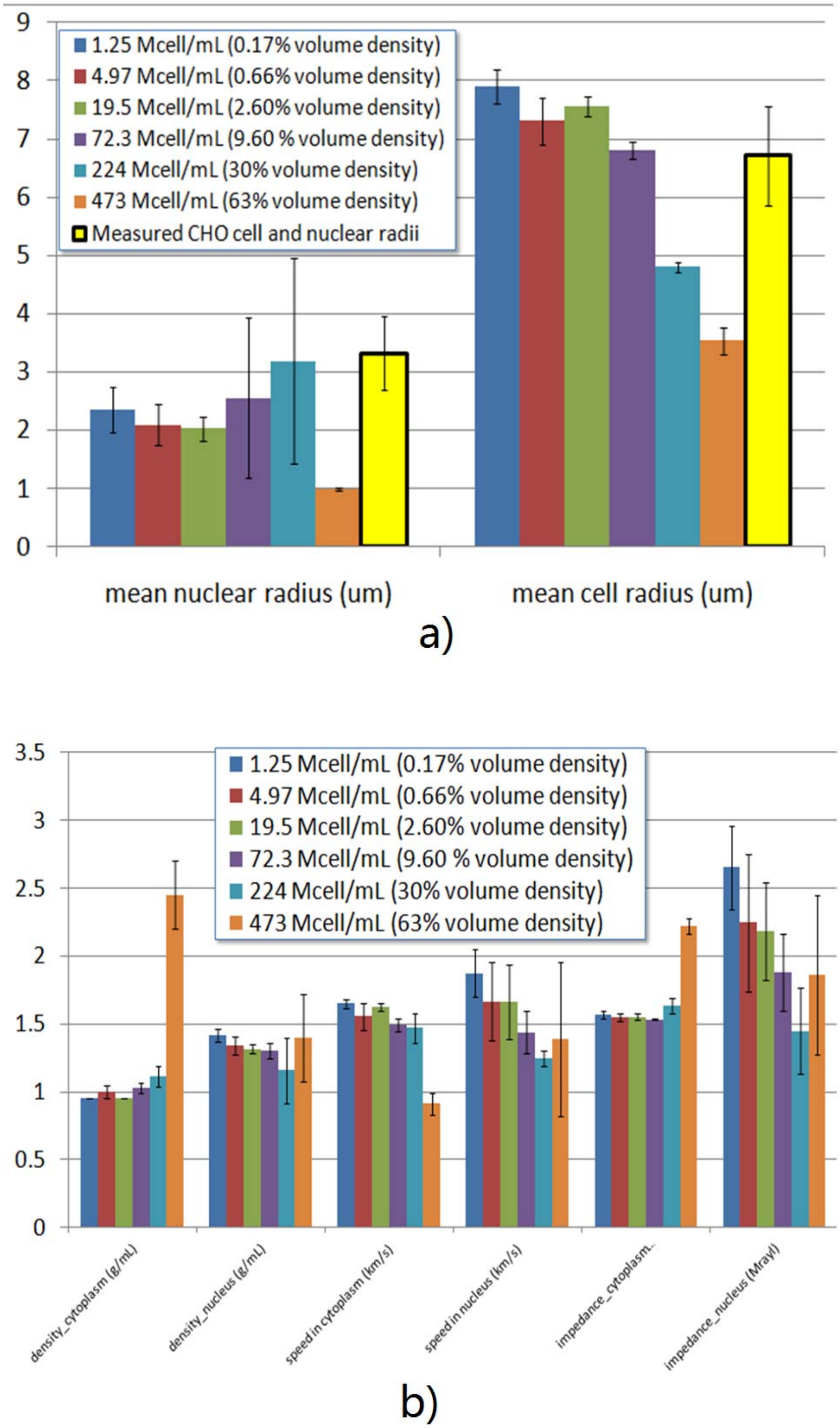

Figure 4.5: Summary of the estimated fit parameters of the CHO cells given by the theoretical concentric sphere BSC calculations: (a) estimated vs. measured nuclear and cell radii, (b) estimated acoustic properties of the cell nucleus and cytoplasm.

(224, 473 Mcell/mL), the cell radius has been underestimated. In fact, Figure 4.5(a) shows that the estimated cell radius decreases as the cell concentration increases except for the 19.5 Mcell/mL case (7.9, 7.3, 7.6, 6.8, 4.8, 3.6 μm for 1.25, 4.97, 19.7, 72.3, 224, 473 Mcells/mL cell pellets, respectively). The underestimate of the cell radius when the cell concentration is large suggests that at high cell concentration either the cells can no longer be modeled as concentric spheres (structural and shape changes) or the total intensity cannot be calculated as the sum of the individual cell intensities (coherent scattering and multiple scattering). Either way indicates that the concentric spheres model is not accurate for large cell concentrations.

The fitted parameters of 473 Mcell/mL cell pellets look very different from those of other concentrations. Those values are actually beyond the range of reasonable values. For instance, the estimated density of cytoplasm is greater than 2 g/mL, and the estimated sound speed in cytoplasm is less than 1000 m/s. Those values are not in agreement with density and sound speed in water. Because the cytoplasm contains mainly water, reasonable properties of cytoplasm should be close to those of sea water, as is also shown by the estimates from cell pellets of other concentrations. The deviation of estimated parameters from reasonable values at high cell concentration is a further indication that at high cell concentration either the cells can no longer be modeled as concentric spheres or the total intensity cannot be calculated as the sum of the individual cell intensities.

4.5 BSC Magnitude versus Number Density

Besides frequency dependence, the magnitude of BSC also appears to provide important information. The BSC magnitude increases with cell concentration, as is qualitatively shown in Figure 4.3. In fact, Equation (2.2) predicts that BSC is proportional to number density. To investigate whether that prediction is observed, the BSC along with a power law fit (at three frequency points 30, 60, 90 MHz) is plotted as a function of number density in Figure 4.6. The fitted power exponent is an indicator of how BSC changes with number density. If BSC is proportional to number density, then the fitted power exponent will be 1. Figure 4.6 shows that the fitted power exponent is smaller than 1 at 30 and 90 MHz, while it is close to 1 at 60 MHz, which indicates that BSC is actually not proportional to number density for all frequencies. The fitted power exponent as a function of frequency in a broad frequency range is displayed in Figure 4.7. The curve appears to be three discontinuous segments because data from different transducers are used. The data from the 40 and 80 MHz transducers are used for the left and right curves respectively, whereas the middle curve is determined using the data from both transducers.

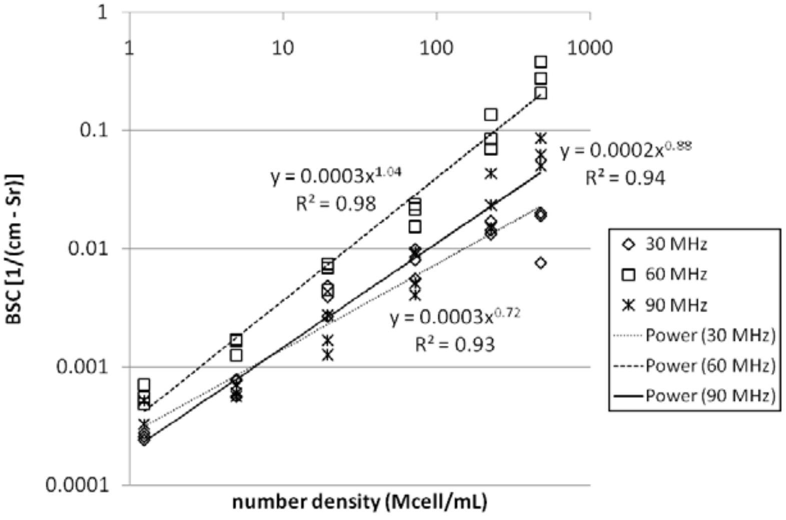

Figure 4.6: BSC magnitude vs. number density. Three frequency points are selected for demonstration: 30, 60 and 90 MHz. The dots are measured data. At each frequency, there are three data points per number density. The lines are power law fitted lines.

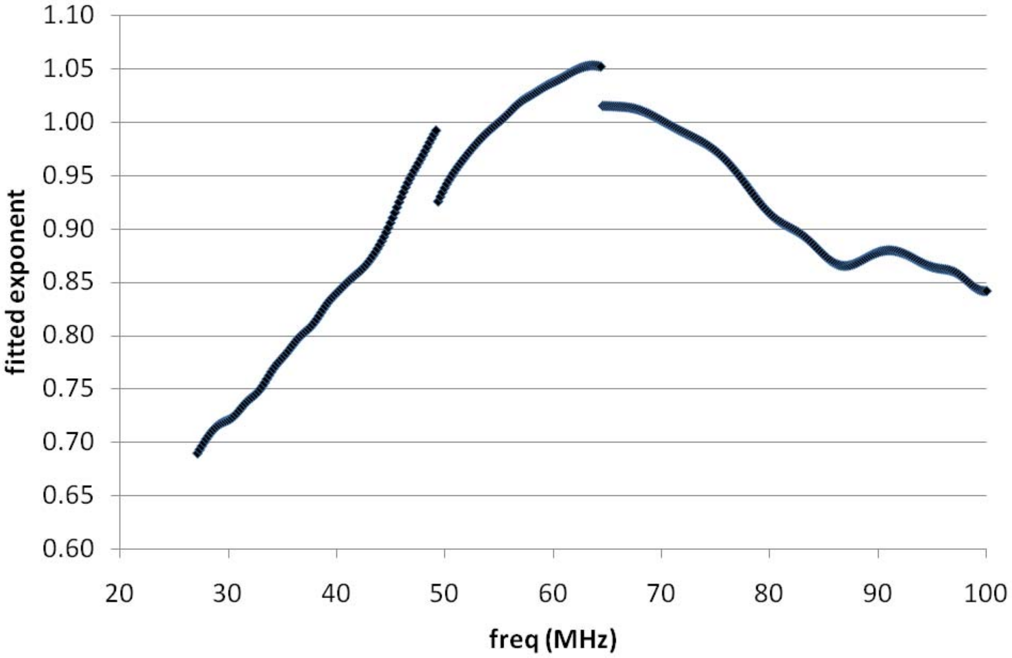

Figure 4.7: Fitted power exponent as a function of frequency for the CHO cell pellets.

The observed BSC versus concentration relationship (fitted power exponent being smaller than 1) at low frequency has been found previously in blood characterization and physical phantom studies. For instance, Shung et al. found that the backscattered power drops when the concentration of erythrocytes in blood surpasses 30% [20]. A similar finding was also reported by Chen et al. for physical phantoms [21]. Those previous findings are in the Rayleigh region and have been attributed to coherent scattering because when the scatterer volume fraction is high, the assumption of a random distribution of scatterers fails due to the correlation among the scatterers. Thus the BSC versus concentration relationship at low frequency (Rayleigh region) found in our experiment might also be attributed to coherent scattering. What is new in our result is that at 60 MHz where the wavelength is comparable to cell size ($ka \approx \pi / 2$, where a is the cell radius), the BSC increases linearly or even faster (fitted power exponent is 1.04) as the concentration becomes high. At 90 MHz, the BSC starts to increase slower again for high concentrations. Therefore, instead of simply decreasing BSC as in the case of Rayleigh scattering, the cell concentration has a more complicated effect on BSC when wavelength is comparable to the scatterer size.

4.6 Discussion and Summary

The backscatter coefficient from cell pellet biophantom is measureable and leads to consistent results. When the cell concentration is low, the comparison of the concentric sphere model with the experimental data from the cell samples shows remarkable agreement. The concentric sphere model is able to provide estimates of cell and nuclear radii, density and speed of sound in the nucleus and cytoplasm respectively.

The shape of measured BSC versus frequency curves, the least-squares concentric sphere model estimates and the observed BSC magnitude versus number density relationships all suggest that the concentric sphere model starts to break down at high cell concentration because the acoustic scattering becomes more complicated. There are a number of possible explanations for this observation. First, coherent scattering may play a role because the assumption of random position of cells may no longer be true as the cells get close to each other. The possible regularity of cell positions can have either a constructive or destructive effect on the total scattered energy depending on the frequency. Using this hypothesis, we may conclude that the effect of coherent scattering is mainly destructive at 20-100 MHz, except for the frequencies around 60 MHz (Figure 4.7). Second, the scattering site may start to change. The background medium becomes isolated by cells, which makes it possible that the background medium effectively becomes the scattering source. Third, multiple scattering may also play a role considering how close the cells are to each other. Additionally, the shape of cells may start to change when they get closer to one another.

The above results and discussion have suggested that the concentric sphere model is not applicable at high concentrations. When does the model start to be affected by the high concentration effect and yield incorrect parameter estimates? From the result of CHO cell pellets, the parameter estimate of the 72.3 Mcell/mL (volume density 10%) does not seem to be affected, while the parameter (cell radius) estimate of the 224 Mcell/mL (volume density 30%) cell pellets is affected (estimated cell radius is smaller than the real value). Therefore the critical volume density should lie between 10% and 30%.

CHAPTER 5

RESULTS – 3T3 CELL PELLETS

In addition to CHO cells, another cell line, the 3T3 cell, is studied. The 3T3 cells and the CHO cells share a similar geometry. However, the size and presumably the acoustic properties of the 3T3 cells are different from those of the CHO. In this chapter, two groups of 3T3 cells, the new and the old, are studied. The two groups are studied because they have significantly different sizes (Figure 2.2(b)) but might share similar acoustic properties since they are both 3T3 cells.

5.1 Cell Concentration

Twelve new 3T3 cell pellets of four different cell concentrations were evaluated. Also, six old 3T3 cell pellets of two different cell concentrations were evaluated. There are three realizations per number density for either case. The cell concentration is represented by number density and volume density as well (Table 5.1).

The cell concentration is also presented by the histology photos in Figure 5.1 and Figure 5.2.

5.2 Cell Pellet Attenuation

Table 5.1: Summary of cell concentrations of the new and old 3T3 cell pellets

	Cell type	Number density (Mcell/mL)	Volume density (mL/mL)
Concentration 1	New 3T3	1.24	0.008
Concentration 2	New 3T3	4.84	0.032
Concentration 3	New 3T3	17.7	0.117
Concentration 4	New 3T3	52.3	0.347
Concentration 5	Old 3T3	4.93	0.014
Concentration 6	Old 3T3	19.0	0.052

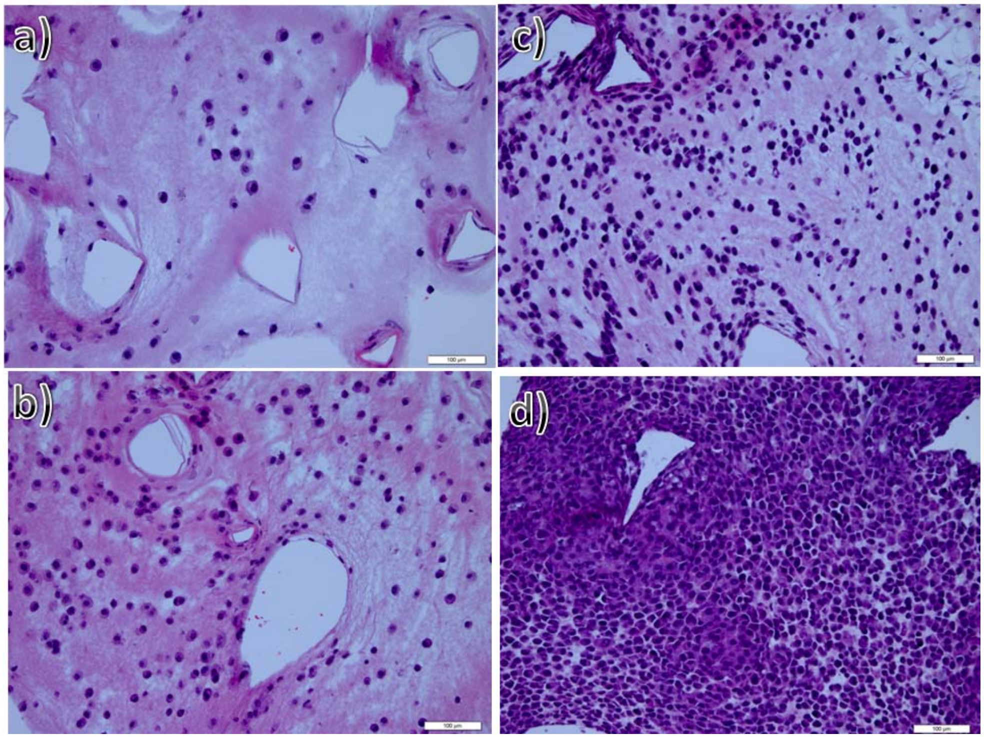

Figure 5.1: Optical microscope images (40X) of H&E stained new 3T3 cells from new 3T3 cell pellets of number density 1.24, 4.84, 17.7, 52.3 Mcell/mL respectively (a-d). Scale bars represent 50 µm.

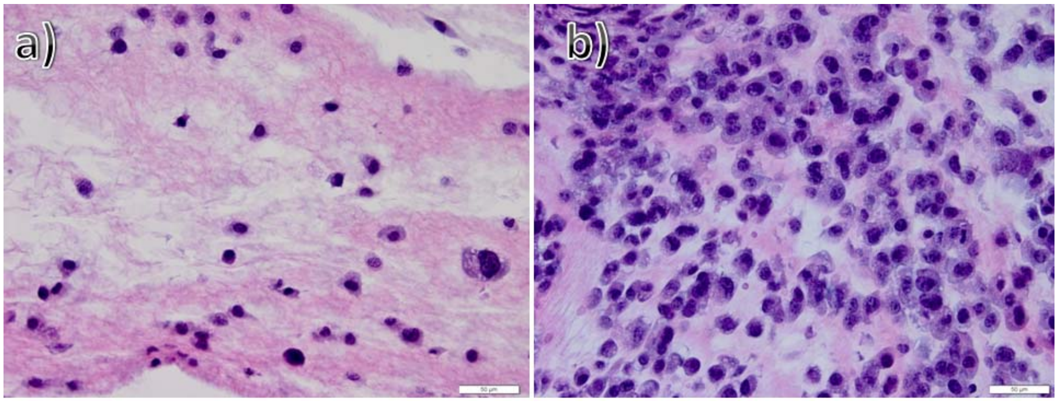

Figure 5.2: Optical microscope images (40X) of H&E stained old 3T3 cells from old 3T3 cell pellets of number density 4.93, 19.0 Mcell/mL respectively (a-b). Scale bars represent 50 µm.

The cell pellet attenuation versus frequency curves of the new 3T3 cell pellets at various cell concentrations are shown in Figure 5.3. Similarly to the CHO cell pellet, the low concentration (1.24, 4.84, 17.7 Mcell/mL) new 3T3 cell pellets have attenuation curves that are very close to the 0 Mcell/mL curve. For that reason, the attenuation of the old 3T3 cell pellets is assumed to be the same as that of the new 3T3 cell pellet of the same number density.

Equation (4.2) is fitted to the 3T3 cell pellet attenuation versus frequency curves. The fitted parameters β and n for various concentrations are listed in Table 5.2.

5.3 BSC versus Frequency

BSC estimates of all the new 3T3 cell pellets are shown in Figure 5.4. Similar to the results of CHO, the BSC versus frequency curves of the new 3T3 cell pellets for different concentrations share a similar pattern in the sense that a consistent peak (crest) is followed by a consistent peak (trough). What is different between the CHO and the new

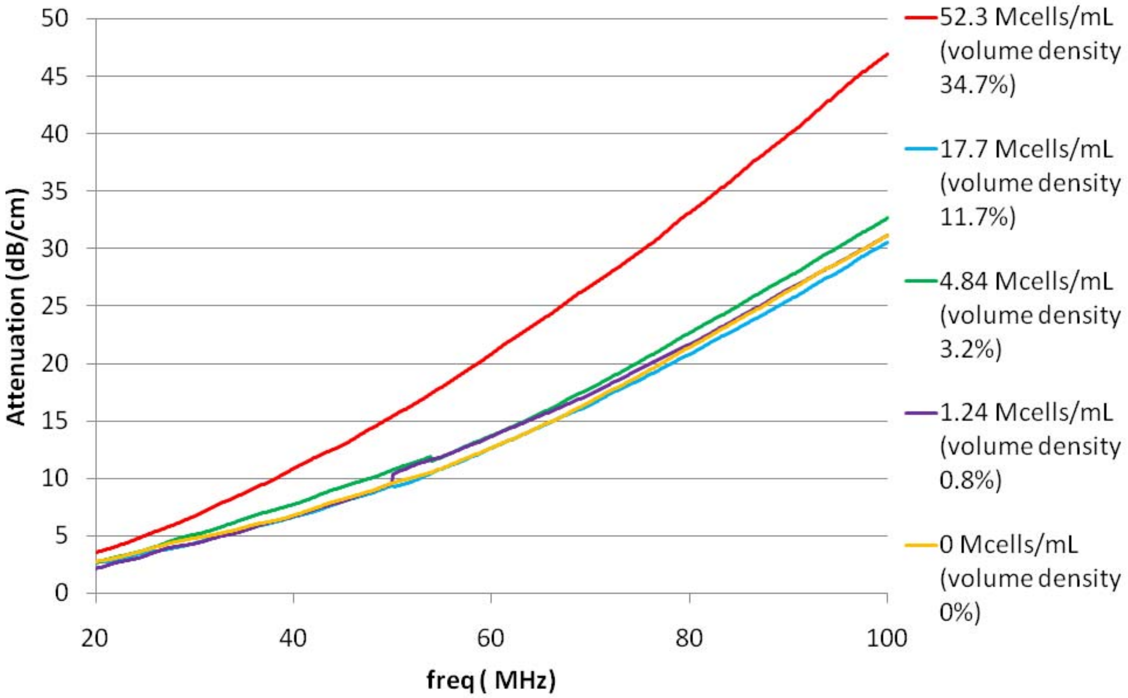

Figure 5.3: New 3T3 cell pellet attenuation versus frequency.

Table 5.2: Summary of the new 3T3 cell pellets attenuation coefficient for various cell concentrations

Number density(Mcell/mL)	β	n
1.24	0.016	1.6
4.84	0.019	1.6
17.7	0.013	1.7
52.3	0.029	1.6

3T3 is the positions of the peaks. For the CHO, the crest is at around 55 MHz and the trough is at around 90 MHz, whereas the crest and the trough are at around 40 MHz and 80 MHz respectively for the new 3T3 (Figure 5.5). This observation is consistent with the fact that the new 3T3 cells are bigger than the CHO cells. Again similar to what is observed with the CHO, the BSC magnitude increases with number density for the new 3T3. However, the shape of BSC curves is almost independent of the number density for the new 3T3. The high concentration effect on the shape of the BSC curve is not obvious

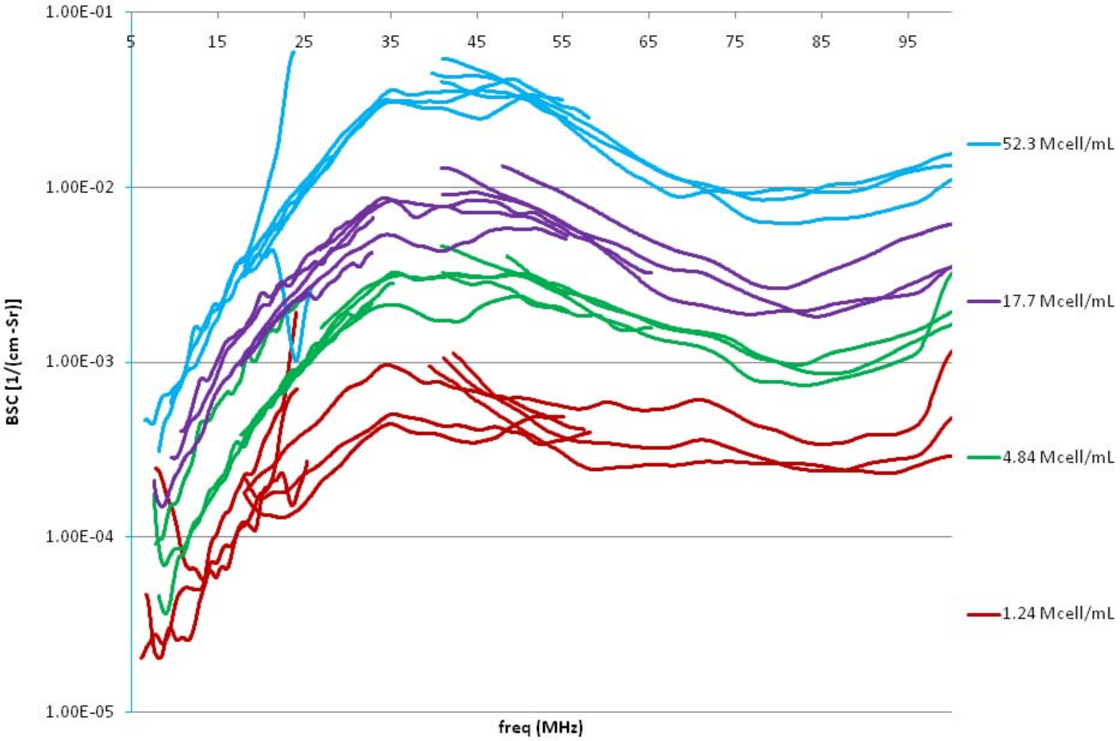

Figure 5.4: Estimated BSC vs. frequency for the new 3T3 cell pellets. Estimated BSC of each cell pellet sample is based on data acquired from three transducers: 20, 40 and 80 MHz. There are three cell pellets per number density.

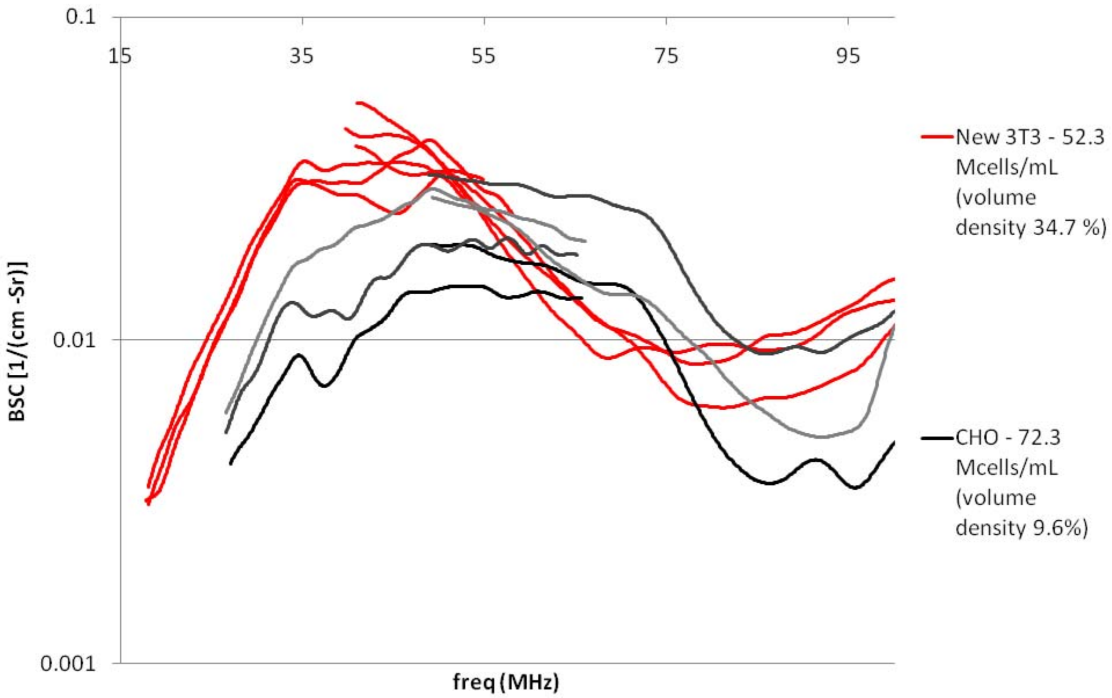

Figure 5.5: Comparison between the estimated BSC vs. frequency for the CHO and for the new 3T3 cell pellets.

for the new 3T3, possibly because the concentration used for the new 3T3 in this study is not high enough to cause the high concentration effect.

BSC estimates of all the old 3T3 cell pellets, in comparison with those of the new 3T3 cell pellets, are shown in Figure 5.6. It is observed in both Figure 5.6(a) and Figure 5.6 (b) that the structures of the BSC curves are almost identical at below 75 MHz for the new and the old 3T3 cell pellets. Those curves start to deviate at about 80 MHz. For above 80 MHz, the new 3T3 curves increase rapidly, whereas the old 3T3 curves are much flatter. This is an indicator that the trough of the old 3T3 curve occurs at a higher frequency point than CHO, which is consistent with the fact that the old 3T3s are smaller than the new 3T3 cells.

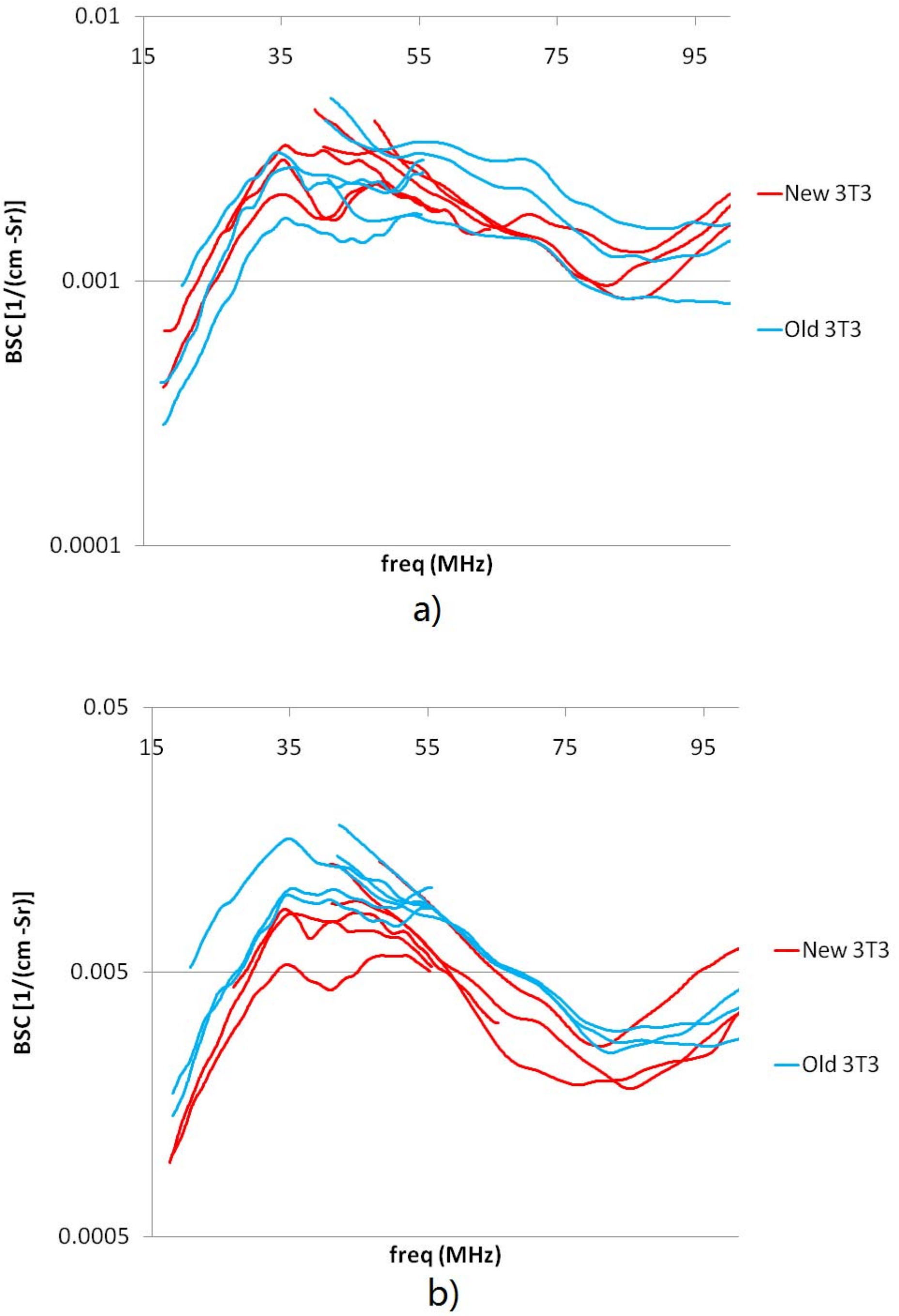

Figure 5.6: Comparison of the BSC as a function of frequency for new and old 3T3 cell pellet biophantoms. (a) The number densities of the new and old 3T3 cell pellets are 4.84 and 4.93 Mcells/mL, respectively. The volume densities of the new and old 3T3 cell pellets are 0.032 and 0.014, respectively. (b) The number densities of the new and old 3T3 cell pellets are 17.7 and 19.0 Mcells/mL, respectively. The volume densities of the new and old 3T3 cell pellets are 0.117 and 0.052, respectively.

5.4 Least-Squares Parameter Estimates

The best fit theoretical BSCs of all 3T3 cell pellets are calculated using the least-squares technique. The estimated parameters of the concentric sphere model for the new 3T3 cells are summarized in Figure 5.7. The mean values are averages of the three cell pellets for each cell concentration. The standard deviations are also calculated based on the three samples per concentration. The estimated parameters of the concentric sphere model for the old 3T3 cells compared to the CHO and the new 3T3 cells are shown in Figure 5.8 and Figure 5.9. Note that in those two figures, the estimated parameters for each of the three realizations per number density are displayed.

The estimated values of cell radius and nuclear radius are comparable to the directly measured values for both the new and old 3T3 cells. Also, we see the trend that the estimated cell radius for the new 3T3 decreases as the cell concentration increases (11.4, 9.1 10.7, 8.4 μm for 1.24, 4.84, 17.7, 52.3 Mcell/mL cell pellets, respectively), which is observed earlier from the CHO.

In order to compare the acoustic properties of the cytoplasm and the nucleus for the CHO and the new 3T3, the average estimates across cell concentrations are shown (Figure 5.10). Note that the average is obtained from the data of the lowest four cell concentrations for CHO, and from the data of all cell concentrations for the new 3T3. The CHO and new 3T3 have very similar estimated parameters (speed of sound, density and acoustic impedance) for the cytoplasm but different estimated parameters for the nuclei.

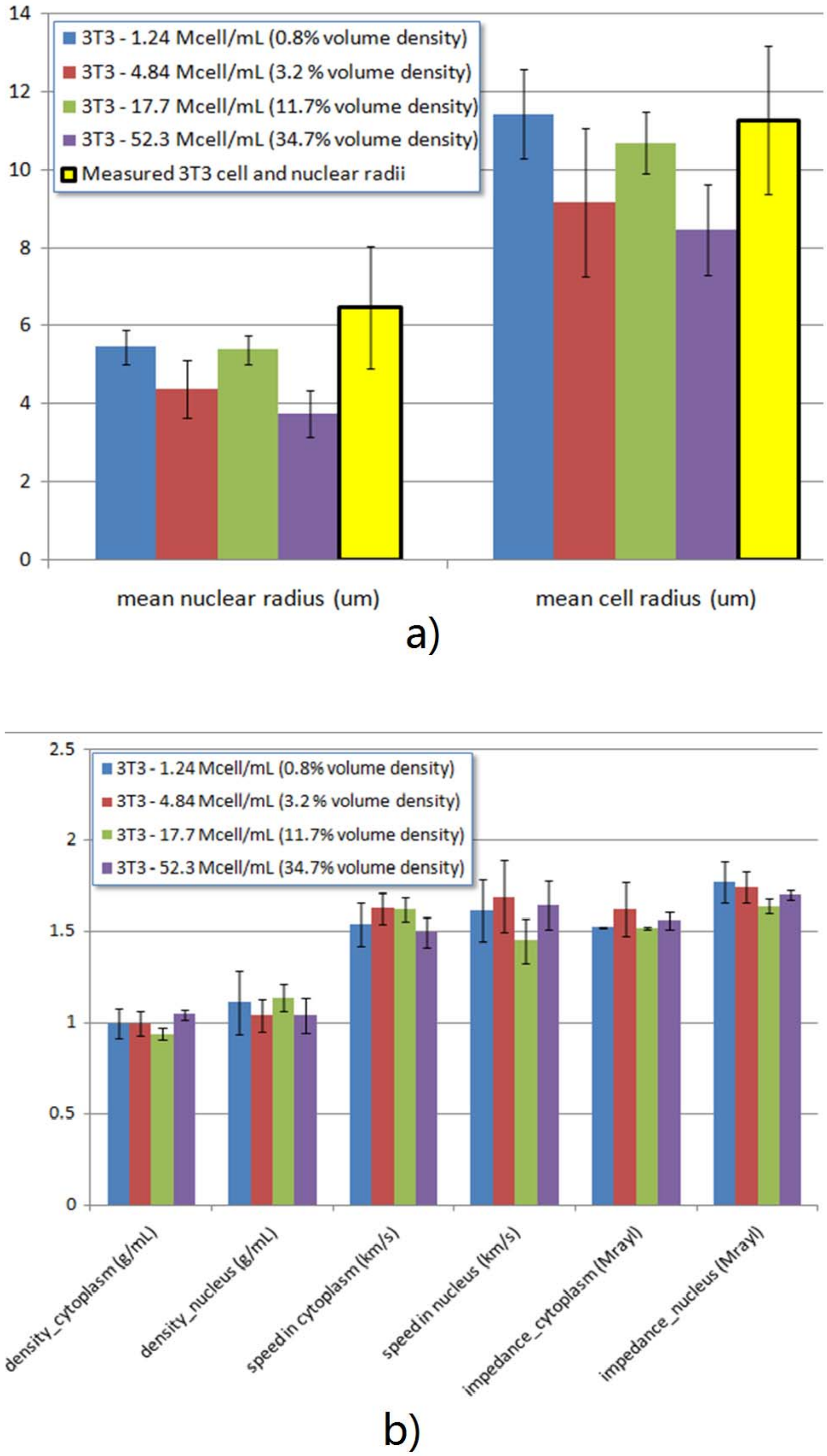

Figure 5.7: Summary of the estimated fit parameters of the new 3T3 cells given by the theoretical concentric sphere BSC calculations: (a) estimated vs. measured nuclear and cell radii, (b) estimated acoustic properties of the cell nucleus and cytoplasm.

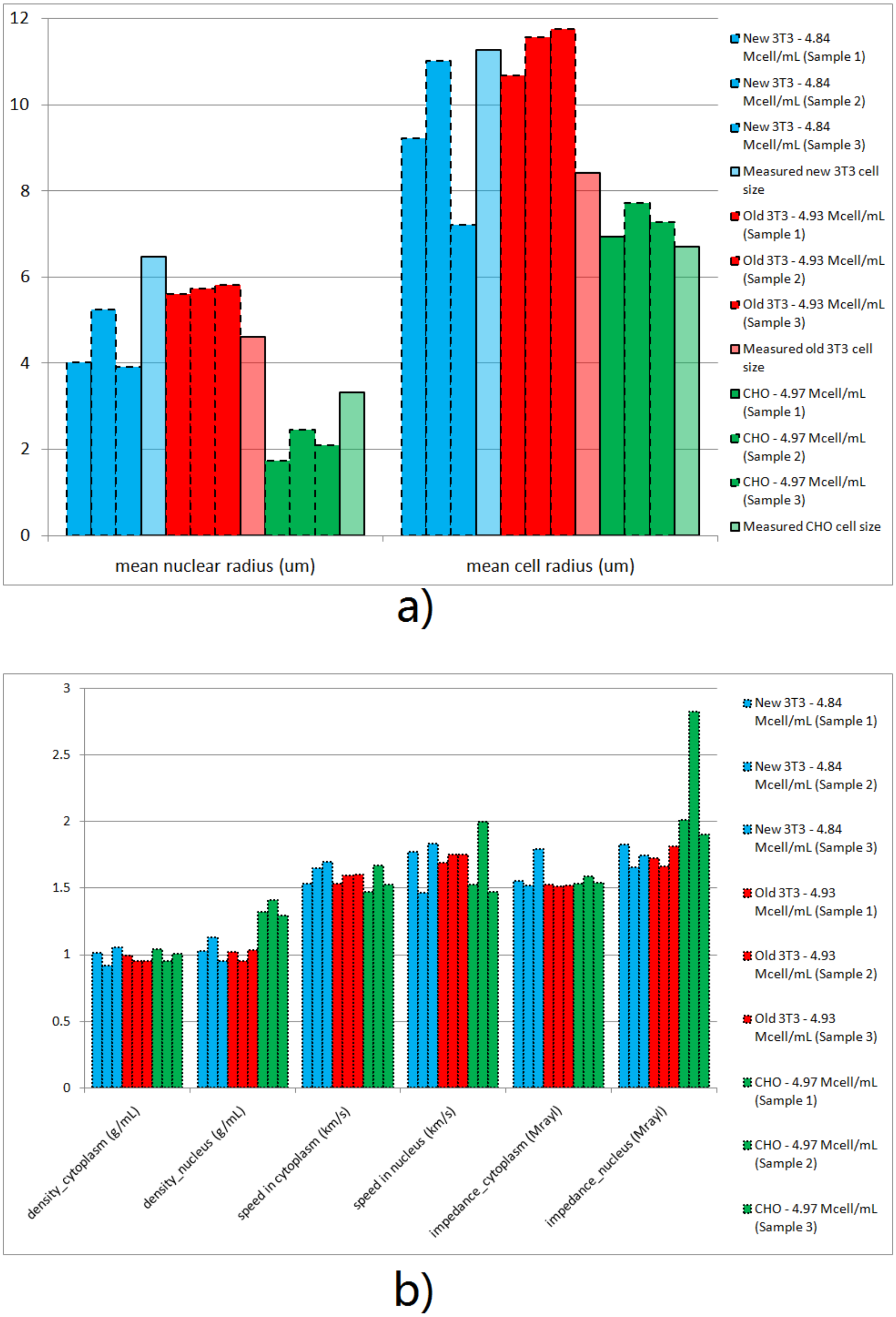

Figure 5.8: Comparison of the estimated fit parameters of the CHO, the old and the new 3T3 cells given by the theoretical concentric sphere BSC calculations for a number density close to 5 Mcell/mL: (a) estimated vs. measured nuclear and cell radii, (b) estimated acoustic properties of the cell nucleus and cytoplasm.

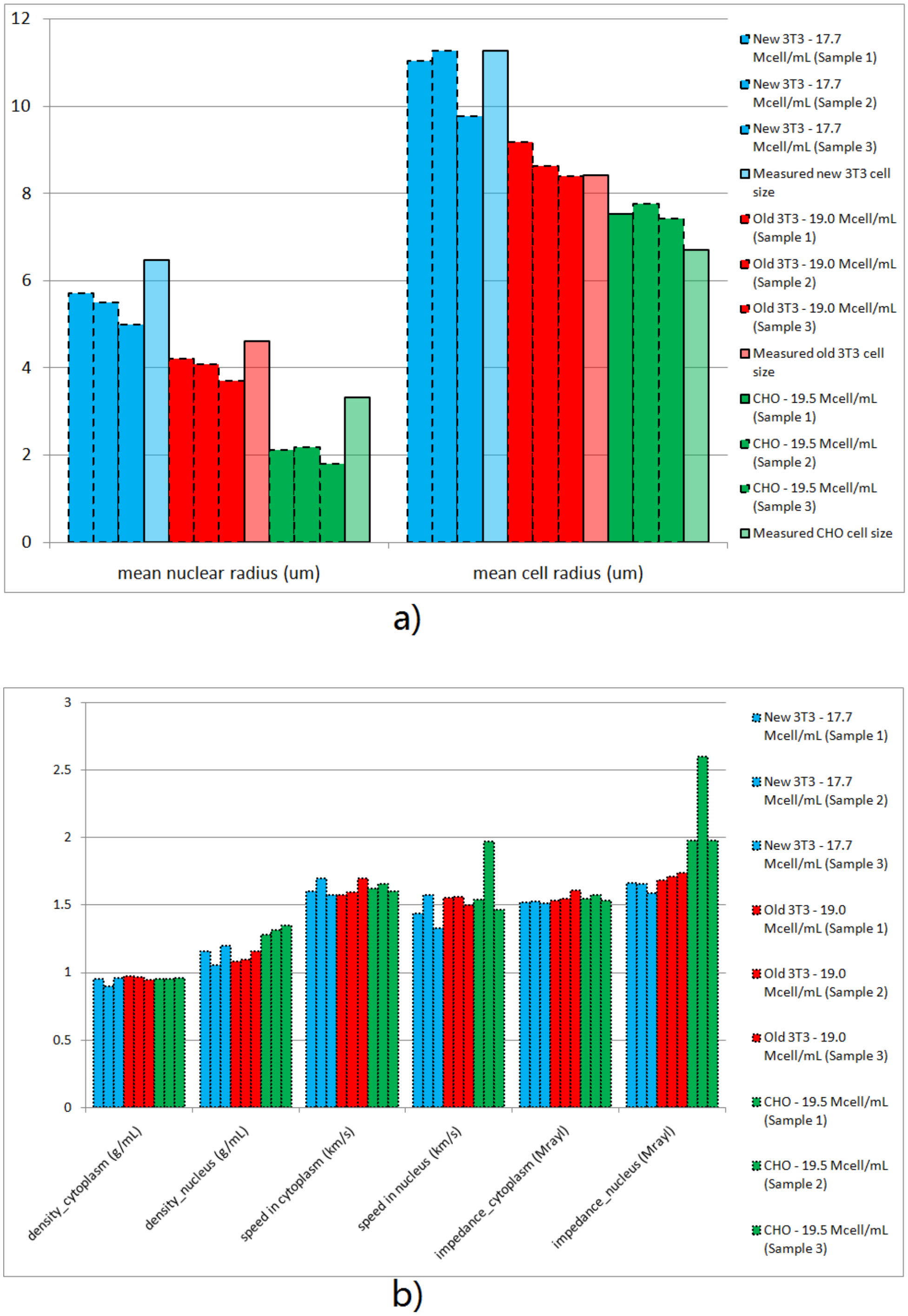

Figure 5.9: Comparison of the estimated fit parameters of the CHO, the old and the new 3T3 cells given by the theoretical concentric sphere BSC calculations for a number density close to 19 Mcell/mL: (a) estimated vs. measured nuclear and cell radii, (b) estimated acoustic properties of the cell nucleus and cytoplasm.

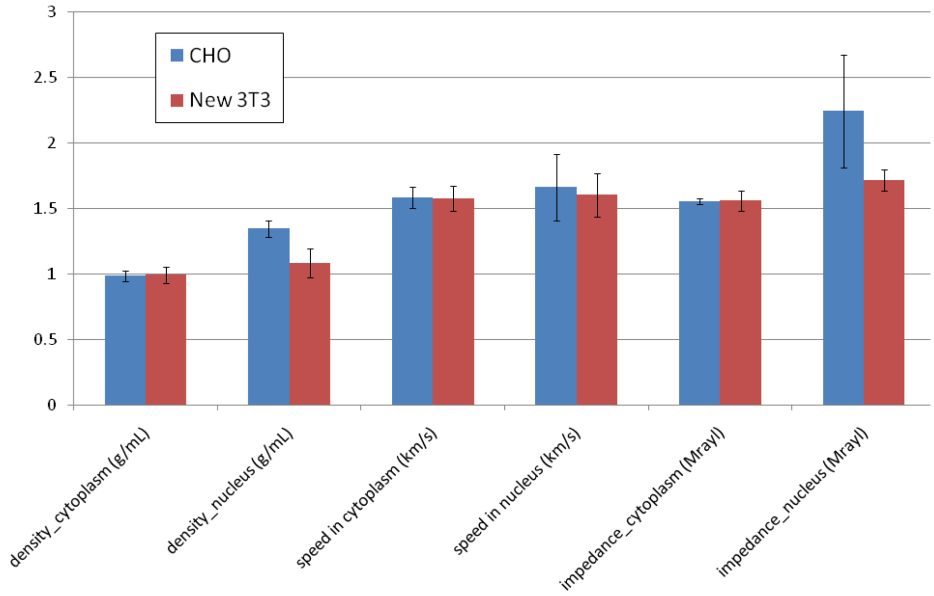

Figure 5.10: Comparison of the average estimated acoustic properties of the CHO and new 3T3 cells.

5.5 BSC Magnitude versus Number Density

The BSC magnitude of the new 3T3 increases with cell concentration, as is qualitatively shown in Figure 5.4. In fact, Equation (2.2) predicts that BSC is proportional to number density. The power law fit of the BSC versus number density relationship for new 3T3 was performed at each frequency point. The fitted power exponent is plotted as a function of frequency (Figure 5.11). The fitted power exponent for CHO is smaller at lower frequencies than that for the new 3T3, which makes sense because the highest cell concentration of the CHO cell pellets is higher than that of the 3T3. The BSC magnitude versus number density is more linear at lower number densities.

Comparing Figure 4.7 and Figure 5.11, we may conclude that the positions of the peaks in the fitted power exponent versus number density curves are correlated to the size of the cells. For example, the peak (crest) for the CHO is at around 60 MHz, 10 MHz higher than the peak (crest) for the new 3T3 curve, while CHO is smaller than the new 3T3 cell.

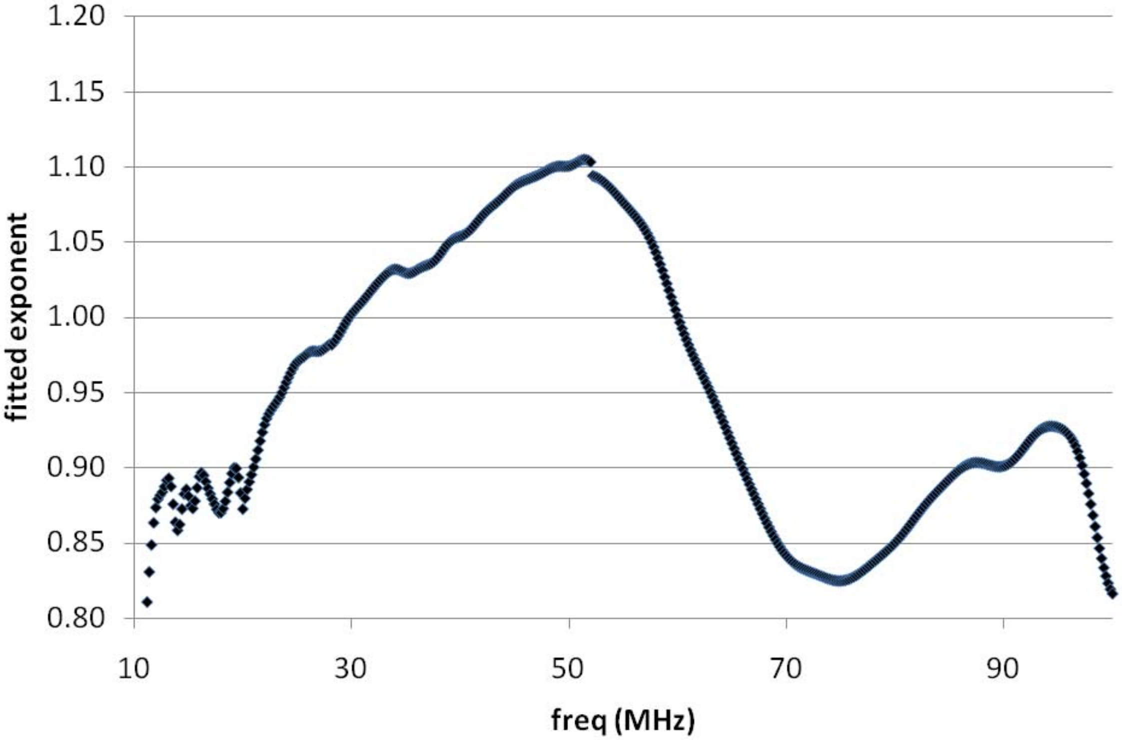

Figure 5.11: Fitted power exponent as a function of frequency for the new 3T3 cell pellets.

5.6 Discussion

The study on 3T3 cell pellets further suggested that (1) the backscatter coefficient from cell pellet biophantom is measureable using single element transducers, (2) the concentric sphere model is applicable when the cell concentration is low, and (3) the concentric sphere model is able to provide estimates of cell and nuclear radii, and of the density and speed of sound in the nucleus and cytoplasm respectively.

While the BSC versus frequency curves of the CHO and the new 3T3 cell pellets are significantly different as expected (Figure 5.5) due the difference between CHO and new 3T3 in both size and acoustic properties, the BSC versus frequency curves of the new and old 3T3 cell pellets are unexpectedly similar (Figure 5.6). It is already known that the new 3T3 cells are significantly bigger than the old. If the sound speed and density of the nucleus and cytoplasm are the same for the old and the new 3T3 cells provided that their sizes are different, their BSC versus frequency curves will, according to the concentric sphere theory, be different. Therefore, the overly similar BSC versus frequency curves of the new and the old 3T3 cell pellets need to be further investigated and explained.

CHAPTER 6

DISCUSSION

6.1 Acoustic Properties of the Cell Nucleus and Cytoplasm

The concentric sphere model yields the sound speed, density and acoustic impedance of both cell nucleus and the cytoplasm for different cell lines (Figure 5.8(b), Figure 5.9(b) and Figure 5.10). This section reviews the acoustic property values in the literature and compares them to our results.

The density of the nucleus may be estimated by analyzing its components. By estimates, 71 % of the volume of the nucleus is occupied by chromatin [15], which is composed of 50% DNA and 50% protein by volume. The densities of DNA and protein are 1.71 g/cm^3 and 1.35 g/cm^3, respectively [15]. If we assume that the remaining 29% volume of the nucleus is an equal combination of dilute brine (1 g/cm^3) and protein, the density of the nucleus will be calculated to be 1.43 g/cm^3 [15]. In terms of speed of sound, Hakim et al. experimentally determined the speed of sound in DNA to be 1830 – 2300 m/s [22], whereas Dukhin et al. estimated the speed of sound in the protein fraction of a single erythrocyte to be 2500 m/s [23]. Those values are high compared to the value of 1500 m/s in water. Taggart et al., however, obtained the speed of sound in isolated nuclei of the acute myeloid leukemia cells and human epithelial kidney cells to be from 1493 m/s to 1549 m/s [24], which is close to the speed of sound in water.

Cellular cytoplasm is mostly composed of a low concentration saline and assumed to have the same sound speed and density as sea water. Berovic et al. used Brillouin scattering to measure the speed of sound along relaxed single fibres of glycerinated rabbit psoas muscle, and observed a wave with a velocity of 1508±7 m/s, which is attributed to sound waves in intra-cellular saline [25]. Other researchers have estimated the speed of sound and density in cytoplasm by examining cells with small nucleus and assuming the speed of sound and density in the whole cell to be the same as those in cytoplasm. For example, it has been reported that the sound speed in bovine aortic endothelial cells in suspension is 1560 m/s [26], in biological cells 1600–1850 m/s [27], in blood cells 1700 m/s [23], in acute myeloid leukemia cells and human epithelial kidney cells 1522–1535 m/s [24], and in myeloid leukemia cells (MCF-7) 1557–1613 m/s [28]. It has also been reported that the density is 1.05–1.11 g/cm^3 for myeloid leukemia cells [29], 1.08 g/cm^3 for bovine aortic endothelial cells in suspension [26], and 9.94–1.016 g/ cm^3 for MCF-7 breast cancer [28].

The results of our study show that the sound speed and density of cytoplasm are consistent with those reported in the literature. Also, the results show that the sound speed and density are larger in the nucleus than in the cytoplasm, which is consistent with the results in [15].

6.2 Comparison to Single Cell Studies

The experimental BSC curves obtained in this study are comparable to the measured backscatter frequency responses in single cell studies (Figure 6.1). All the curves show peaks in the frequency domain and are consistent with the theoretical predictions shown

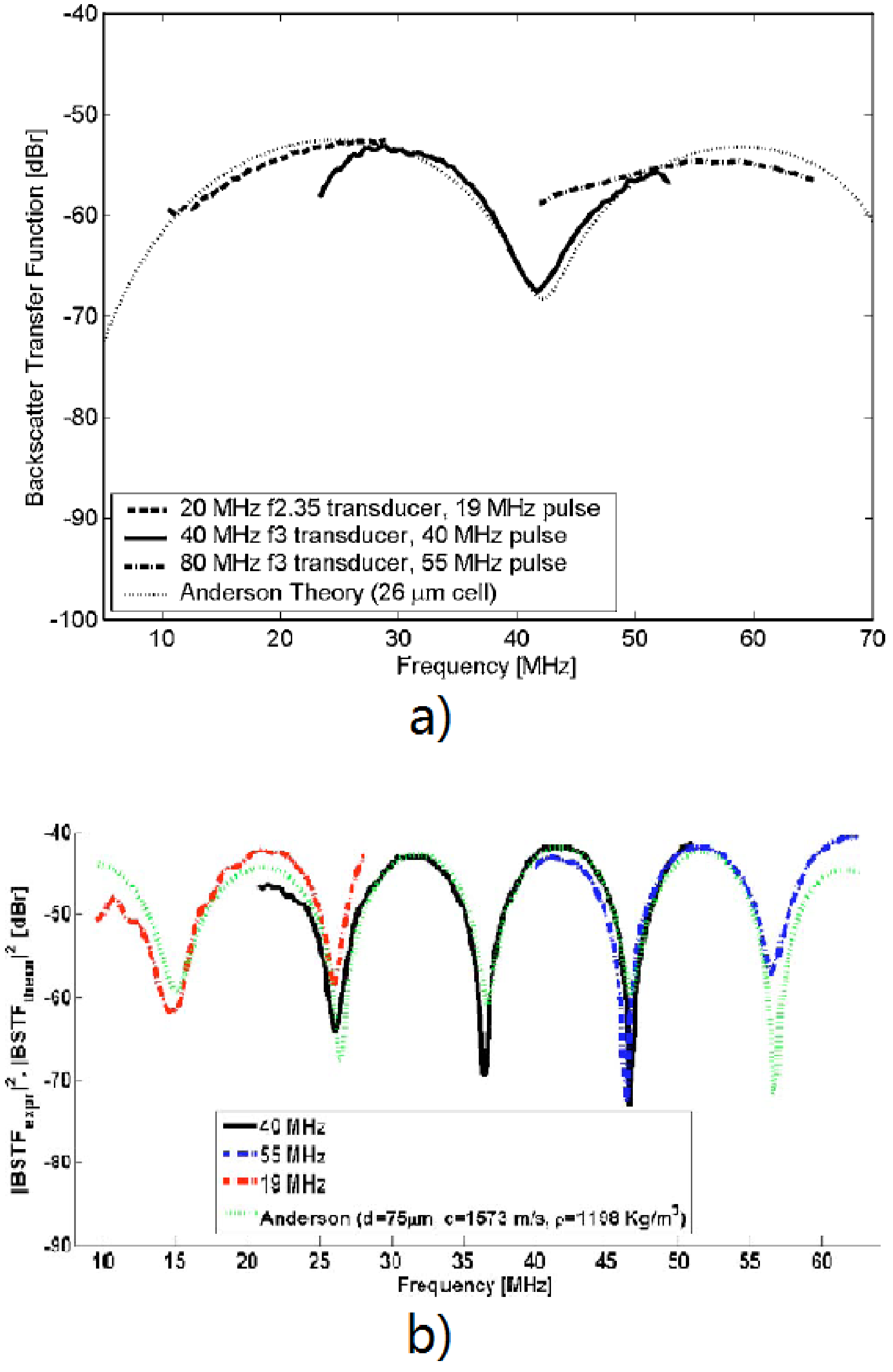

Figure 6.1: Measured backscatter frequency response from: (a) single PC-3 cells in phosphate buffered saline solution and (b) single sea urchin oocytes in seawater. (a) is adapted from Fig. 3-a in [30]. (b) is adapted from Fig. 3 in [31]. The experimental curves were measured using high-frequency transducers.

in Figure 2.4. Figure 2.4 predicts that the dips in the frequency response from monodispersed cells or single cell are sharp, a prediction confirmed by Figure 6.1. Figure 2.4 also predicts that the dips in the frequency response will be shallower if the cells are polydispersed. This prediction is confirmed by all the BSC curves from CHO and 3T3 cell pellets.

6.3 Comparison of Models

As introduced in Section 1.2, there are a number of models for ultrasonic scattering from cells: the spherical Gaussian model, the Anderson model, the fluid field sphere model, the New Cell Model, the concentric sphere model, etc. The Gaussian model has been used most widely, but lacks physical foundation. The fluid field sphere model is a mathematically simplified version of the Anderson model, whereas the New Cell Model takes into account the biological structure of the cell cytoplasm. Both the fluid field sphere model and the New Cell Model require that the impedance mismatch between the scatterers and the background is small, which is not necessarily the case for cells based on the discussion in Section 6.1. The Anderson model and the concentric sphere model deal with accurate solutions of the acoustic scattering problems and do not have the small impedance mismatch requirement.

The Anderson model assumes a fluid scatterer, which in reality can be either the cell or the nucleus, thus leading to the question of what the prominent scattering site is for the Anderson model. While there is evidence supporting either the nucleus or the cell as the prominent scattering site depending on the type of cell studied, the interpretation of the model and the estimated parameters can still be ambiguous. Those problems do not appear in the concentric sphere model. Instead of trying to determine whether the cell or the nucleus is playing a prominent role in acoustic scattering, the concentric sphere model takes into account of the contributions from both. Hence the property estimates can be obtained for both the nucleus and the cytoplasm. The concentric sphere model seems to be superior to other models in that sense.

CHAPTER 7

CONCLUSIONS AND FUTURE WORK

7.1 Summary and Conclusion

The ultrasonic backscatter coefficients have been measured for the CHO, and for the new and the old 3T3 cells of various cell concentrations using high frequency single element focused transducers. This study shows that the backscatter coefficients from such biophantoms are measurable. The results of BSC are accurate and repeatable. The BSC curves from the low cell concentration biophantoms (volume density < 30 %) agree well with the concentric sphere model; the magnitude of the BSC increases with number density, and the shape of the BSC curves is consistent among different number densities. Fitting the concentric sphere model to the measured BSC data yields model parameter estimates that are meaningful and agree with physical reality. The results are repeated for multiple cell lines.

The acoustic scattering at high cell concentration is more complicated than that at low concentration. The high cell concentration has a significant impact on the measured backscatter coefficients. The concentric sphere model starts to break down when the cell concentration becomes high. The magnitude and shape of the BSC versus frequency curves are both affected. The model parameter estimates start to deviate from reasonable values; the estimated cell and nuclear radii start to decrease with number density. The critical volume density, starting from when the model becomes inapplicable, is between 10% and 30%.

7.2 Future Work

Although good results have been obtained so far, there is still work to be conducted on the study of biophantoms. Following are a few future directions.

First, the problem of over-similarity between the BSC curves of the new and the old 3T3 cell pellets needs to be investigated.

Second, it is worthwhile separating the cell nucleus and the cytoplasm and measuring the density and speed of sound of each component. On one hand, it will be helpful in addressing the problem mentioned in the previous paragraph. On the other hand, the results of such measurements can be used to verify the estimated acoustic properties from the model.

Third, the issue of high concentration needs to be further investigated. It has been observed that the concentric sphere model does not seem to work well for the high concentration cell pellets. Many possible reasons have been proposed to explain the finding. The real reason needs to be identified. Appropriate mathematical models may need to be developed for the high concentration situation.

Fourth, cells under other conditions need to be studied. For instance, the cells-only condition under which the cells are packed closely without adding plasma and thrombin is worth studying. The so-called cells-only cell pellet has been scanned before. However, the results are not valid because of freezing damage. New experiments need to be done to continue with the cells-only situation. As another example, the effect of size distribution of the cells on the measured BSC, needs to be studied. The results of single cell study are available in the literature; the study of polydispersed cells in this thesis also shows good agreement with the theory. However, results from monodispersed cells that agree with the theory have not been obtained. This agreement is hard to achieve particularly because a strictly monodisperse situation is hard to realize experimentally.

REFERENCES

[1] J. Mamou, M. L. Oelze, W. D. O'Brien Jr., and J. F. Zachary, "Perspective on biomedical quantitative ultrasound imaging," *IEEE Signal Processing Magazine,* vol. 23, pp. 112–116, 2006.

[2] X. Chen, D. Phillips, K. Q. Schwarz, J. G. Mottley and K. J. Parker, "The measurement of backscatter coefficient from a broadband pulse-echo system: A new formulation," *IEEE Transactions on Ultrasonics, Ferroelectrics, and Frequency Control*, vol. 44, pp. 515-525, 1997.

[3] R. A. Sigelmann and J. M. Reid, "Analysis and measurement of ultrasonic backscattering from an ensemble of scatterers excited by sine-wave bursts," *Journal of the Acoustical Society of America*, vol. 53, pp. 1351–1355, 1973.

[4] F. L. Lizzi, M. Greenebaum, E. J. Feleppa, and M. Elbaum, "Theoretical framework for spectrum analysis in ultrasonic tissue characterization," *Journal of the Acoustical Society of America*, vol. 73, pp. 1366–1371, 1983.

[5] J. A. Campbell and R. C. Waag, "Normalization of ultrasonic scattering measurements to obtain average differential scattering cross sections for tissues," *Journal of the Acoustical Society of America*, vol. 74, pp. 393-299, 1983.

[6] E. L. Madsen, M. F. Insana, and J. A. Zagzebski, "Method of data reduction for accurate determination of acoustic backscatter coefficients," *Journal of the Acoustical Society of America*, vol. 76, pp. 913–923, 1984.

[7] M. Ueda, and Y. Ozawa, "Spectral analysis of echoes for backscattering coefficient measurement," *Journal of the Acoustical Society of America*, vol. 77, pp. 38–47, 1985.

[8] G. Yao, V. L. Newhouse and J. Satrapa, "Estimation of scatterer concentration from randomly scattered signals," *Journal of the Acoustical Society of America*, vol. 84, pp. 771–779, 1988.

[9] M. F. Insana, R. F. Wagner, D. G. Brown and T. J. Hall, "Describing small-scale structure in random media using pulse-echo ultrasound," *Journal of the Acoustical Society of America*, vol. 87, pp. 179–192, 1990.

[10] M. L. Oelze and J. F. Zachary, “Examination of cancer in mouse models using high-frequency quantitative ultrasound,” *Ultrasound in Medicine & Biology*, vol. 32, pp. 1639-1648, 2006.

[11] G. J. Czarnota and M. C. Kolios, “Ultrasound detection of cell death,” *Imaging in Medicine*, vol. 2, pp. 17-28, 2010.

[12] D. Nicholas, “Evaluation of backscattering coefficients for excised human tissues: results interpretation, and associated measurements,” *Ultrasound Medicine & Biology*, vol. 8, pp. 17–28, 1982.

[13] M. L. Oelze and W. D. O’Brien Jr., “Application of three scattering models to characterization of solid tumors in mice,” *Ultrasonic Imaging*, vol. 28, pp. 83–96, 2006.

[14] J. Mamou, M. L. Oelze, W. D. O’Brien Jr., and J. F. Zachary, “Identifying ultrasonic scattering sites from three-dimensional impedance maps,” *Journal of the Acoustical Society of America*, vol. 117, pp. 413-423, 2005.

[15] R. E. Baddour, M. D. Sherar, J. W. Hunt, G. J. Czarnota, and M. C. Kolios, “High-frequency ultrasound scattering from microspheres and single cells,” *Journal of the Acoustical Society of America*, vol. 117, pp. 934-943, 2005.

[16] V. C. Anderson, “Sound scattering from a fluid sphere,” *Journal of the Acoustical Society of America*, vol. 22, pp. 426-431, 1950.

[17] J. McNew, R. Lavarello, and W. D. O’Brien Jr., “Sound cattering from two concentric fluid spheres,” *Journal of the Acoustical Society of America*, vol. 125, pp. 1–4, 2009.

[18] M. Teisseire, A. Han, R. Abuhabsah, J. Blue Jr., S. Sarwate, and W. D. O’Brien Jr., “Ultrasonic backscatter coefficient quantitative estimates from Chinese hamster ovary cell pellet biophantoms,” *Journal of the Acoustical Society of America*, vol. 128, pp. 3175–3180, 2010.

[19] F. H. Fisher and V. P. Simmons, “Sound absorption in sea water,” *Journal of the Acoustical Society of America*, vol. 62, pp. 558-564, 1977.

[20] K. K. Shung et al., “Effect of flow disturbance on ultrasonic backscatter from blood,” *Journal of the Acoustical Society of America*, vol. 75, pp. 1265-1272, 1984.

[21] J. Chen and J. A. Zagzebski, “Frequency dependence of backscatter coefficient versus scatterer volume fraction,” *IEEE Transactions on Ultrasonics, Ferroelectrics, and Frequency Control*, vol. 43, pp. 345-353, 1996.

[22] M. B. Hakim, S. M. Lindsay and J. Powell, “The speed of sound in DNA,” *Biopolymers*, vol. 23, pp. 1185–1192, 1984.

[23] A. S. Dukhin, P. J. Goetz, and T. G. M. van de Ven, “Ultrasonic characterization of proteins and blood cells,” *Colloids and Surfaces B: Biointerfaces*, vol. 53, pp. 121-126, 2006.

[24] L. R. Taggart, R. E. Baddour, A. Giles, G. J. Czarnota and M. C. Kolios, “Ultrasound characterization of whole cells and isolated nuclei,” *Ultrasound in Medicine & Biology*, vol. 22, pp. 389-401, 2007.

[25] N. Berovic, N. Thomas, R. A. Thornhill and J. M. Vaughan, “Observation of Brillouin scattering from single muscle fibers,” *European Biophysics Journal*, vol. 17, pp. 69–74, 1989.

[26] M. Boynard, M. P. Wautier, P. Perrotin, and J. L. Wautier, “Mechanical properties of bovine aortic endothelial cells in suspension studied by ultrasonic interferometry,” *European Journal of Ultrasound*, vol. 12, pp. 81-88, 2000.

[27] J. Bereiter-Hahn and C. Blasé, “Ultrasonic characterization of biological cells,” in *Ultrasonic Non-Destructive Evaluation*, T. Kundu, Ed. Boca Raton, FL: CRC Press, 2004, pp. 725-760.

[28] E. M. Strohm and M. C. Kolios, “Measuring the mechanical properties of the cells using acoustic microscopy,” in *31st Annual International Conference of IEEE Engineering in Medicine and Biology Society*, 2009, pp. 6042-6045.

[29] O. Falou, M. Rui, A. E. Kaffas, J. C. Kumaradas and M. C. Kolios, “The measurement of ultrasound scattering from individual micron-sized objects and its application in single cell scattering,” *Journal of the Acoustical Society of America*, vol. 128, pp. 894-902, 2010.

[30] R. E. Baddour and M. C. Kolios, “The fluid and elastic nature of nucleated cells: implications from the cellular backscatter response,” *Journal of the Acoustical Society of America*, vol. 121, pp. 16-22, 2006.

[31] O. Falou, R. E. Baddour, G. Nathanael, G. J. Czarnota, J. C. Kumaradas and M. C. Kolios, “A study of high frequency ultrasound scattering from non-nucleated biological specimens,” *Journal of the Acoustical Society of America*, vol. 124, pp. 278-283, 2008.